ADVANCED FUNCTIONAL MATERIALS

Supporting Information

for *Adv. Funct. Mater.*, DOI 10.1002/adfm.202309653

The Role of the Organic Cation in Developing Efficient Green Perovskite LEDs Based on Quasi-2D Perovskite Heterostructures

Alexandra J. Ramadan, Woo Hyeon Jeong, Robert D. J. Oliver, Junke Jiang, Akash Dasgupta, Zhongcheng Yuan, Joel Smith, Jae Eun Lee, Silvia G. Motti, Olivia Gough, Zhenlong Li, Laura M. Herz, Michael B. Johnston, Hyosung Choi, Jacky Even, Claudine Katan, Bo Ram Lee* and Henry J. Snaith**

Supplementary Information: The role of the organic cation in developing efficient green perovskite LEDs based on quasi-2D perovskite heterostructures

Alexandra J. Ramadan[1,2†], Woo Hyeon Jeong[3†], Robert D. J. Oliver[1,2], Junke Jiang[4], Akash Dasgupta[2], Zhongcheng Yuan[2], Joel Smith[2], Jae Eun Lee[2], Silvia G. Motti[5], Olivia Gough[2], Zhenlong Li[2], Laura M. Herz[2,6], Michael B. Johnston[2], Hyosung Choi[7], Jacky Even[8], Claudine Katan[4], Bo Ram Lee[3]*, Henry J. Snaith[2]**

1. Department of Physics and Astronomy, University of Sheffield, Hounsfield Road, Sheffield, S3 7RH, United Kingdom
2. Clarendon Laboratory, Department of Physics, University of Oxford, Parks Road, Oxford, OX1 3PU, United Kingdom
3. School of Advanced Materials Science and Engineering, Sungkyunkwan University, Suwon 16419, Republic of Korea
4. Univ Rennes, ENSCR, INSA Rennes, CNRS, ISCR – UMR 6226, F-35000 Rennes, France
5. School of Physics and Astronomy, Faculty of Engineering and Physical Sciences, University of Southampton, University Road SO17 1BJ, Southampton, United Kingdom
6. Institute for Advanced Stufy, TU Munich, Lichtenbergstr. 2a, 85748 Garching, Germany
7. Department of Chemistry, Research Institute for Convergence of Basic Sciences, and Research Institute for Natural Science, Hanyang University, Seoul 04763, Republic of Korea
8. Univ Rennes, INSA Rennes, CNRS, Institut FOTON–UMR 6082, Rennes F-35000, France

Corresponding authors: a.ramadan@sheffield.ac.uk, brlee@skku.edu, henry.snaith@physics.ox.ac.uk

†: these authors contributed equally to this work

Experimental Methods

Materials

Indium tin oxide-based transparent conductive electrode (~4.5 Ω/sq ITO) was purchased from AMG. Poly(3,4-ethylenedioxythiophene): poly-styrene sulfonate (PEDOT:PSS, Clevios AI 4083) was purchased from Heraeus Clevios, poly (9-vinlycarbazole) (PVK, M_w=1,100,000 g mol^{-1}), lead bromide ($PbBr_2$, 99.999%), cesium bromide (CsBr, 99.999%), 18-crown-6 (≥ 99.0%, 274984), Polyethylenimine, 80% ethoxylated solution (37 wt.% in H_2O), dimethyl sulfoxide (DMSO, 99.9%) and chlorobenzene (CB, 99.8%) were purchased from Sigma Aldrich. 2,2′,2″-(1,3,5-benzinetriyl) tris(1-phenyl-1-H-benzimidazole) (TPBi, 99.9%) was purchased from OSM. n-butylammonium bromide (BABr) was purchased from Greatcellsolar. Lithium fluoride (LiF, 99.9%), Silver (Ag, 99.99%) and Aluminium (Al, 99.9%) were purchased from iTASCO.

Perovskite thin film fabrication

The following processes were all carried out in a nitrogen filled glovebox. Perovskite precursor solutions were prepared by weighing all of the powders into a single vial, dissolving them in anhydrous DMSO, with 4mg/ml of 18-crown-6, by stirring for 24 h and filtering with a 0.45μm PTFE membrane filter. The masses of all the precursors can be found in **Table S1**. A spin-coating program of 1000 rpm (1000 rpm s^{-1} ramp) for 5 s followed by 3000 rpm for 55 s (3000 rpm s^{-1} ramp) was used. The spin-coater was set up with a plastic collar lined with a lint free wipe surrounding the chuck and run with the lid open (using a magnet to override the interlock). The substrate was placed on the chuck and spun for approximately 2 s before 60 μL of precursor solution was dynamically dispensed onto the spinning substrate. After spincoating 3M scotch tape or a PTFE coated substrate was affixed to the perovskite thin film and the perovskite was annealed for 2.5 minutes at 100 °C after which the scotch tape/PTFE substrate was removed, and the perovskite further annealed for 1 minute. After each film was spin-coated the clean room wipe was replaced to reduce the amount of DMSO in the immediate vicinity of the film during crystallization. We found this critical for the fabrication of reproducible films and devices.

Light emitting diode fabrication

Light emitting diodes were fabricated onto indium tin oxide coated glass substrates with a device architecture of ITO/PEDOT:PSS/PVK/perovskite/TPBi/LiF/Al. Pre-etched indium tin oxide substrates were cleaned by sonication in a 2 v/v% Decon 90 detergent solution, deionised water, acetone and isopropanol for 10 minutes each. The substrates were then dried with N_2 and cleaned in

UV-ozone for 10 minutes. In air, thin films of PEDOT:PSS were deposited onto clean ITO, via spin-coating at 4500 rpm for 40 seconds. These films were annealed at 140 °C for 10 minutes and then transferred into a N_2 filled glovebox. Subsequently thin films of PVK were deposited (4mg/ml in anhydrous chlorobenzene) via spin-coating at 4000 rpm for 40 seconds and annealed at 130 °C for 10 minutes. Perovskite thin films were deposited as described above. Thin films of TPBi (40 nm), LiF (1 nm) and Al (70 nm) were sequentially thermally evaporated.

Electron only device fabrication

Cleaned ITO substrates were treated by UV-ozone for 10 min. A solution of ZnMgO NPs (7 mg/ml in Ethanol) was spin-coated onto the ITO glass at 2500 rpm for 30 s and annealed in air at 150 °C for 10 min. A solution of Polyethylenimine, 80% ethoxylated solution (PEIE) (dissolve in isopropyl alcohol, 0.025% mass ratio) was spin coated onto the ZnMgO film at a speed of 4000 rpm and annealed at 110 °C for 10 min, Then, the substrate was transferred into a N_2 filled glovebox. After that, perovskite thin films were deposited as described above. Thin films of TPBi (40 nm), LiF (1 nm) and Al (70 nm) were sequentially thermally evaporated.

Hole only device fabrication

Cleaned ITO substrates were treated by UV-ozone for 10 min. PEDOT:PSS were deposited onto clean ITO, via spin-coating at 4500 rpm for 40 seconds. These films were annealed at 140 °C for 10 minutes and then transferred into a N_2 filled glovebox. Subsequently thin films of PVK were deposited (4mg/ml in anhydrous chlorobenzene) via spin-coating at 4000 rpm for 40 seconds and annealed at 130 °C for 10 minutes. After that, perovskite thin films were deposited as described above. Thin films of MoO_3 (15 nm), and Ag (100 nm) were sequentially thermally evaporated.

LED characterisation

J-V-L characteristics and device performances were measured using a Konica Minolta spectroradiometer (CS- 2000) with a Keithley 2400 source meter.

Intensity dependent Photoluminescence Quantum Yield (PLQY) measurements

Absolute photoluminescence measurements were performed using the De Mello method.[1] Samples were excited using a continuous wave 450 nm laser diode (Thor Labs) which was coupled into an optical fibre into an integrating sphere where it was used to photoexcite the sample. The intensity of the laser was varied using neutral density filters (Thor Labs). The intensity of the laser was measured with a Si photodiode (818-UV/VV, Newport) and a power meter (843-R-USB, Newport) just before entering the integrating sphere. The light from the integrating sphere was coupled into a second optical fibre and measured using an Ocean Optics QEPro spectrometer. The integrating sphere and

fibre were calibrated by shining a halogen lamp of a known spectrum into the sphere and a spectral correction factor was determined to ensure the detected spectrum of the lamp matched its known spectral irradiance.

Time Correlated Single Photon Counting (TCSPC) measurements

Time Correlated Single Photon Counting Measurements were carried out using (independently) a 400 nm and a 470 nm laser (PicoHarp, LDH-D-C-405M and PicoHarp, LDH-D-C-470M) in pulsed excitation mode with a repetition rate of 500 kHz. The emitted photoluminescence was collected and coupled into a grating spectrometer (Princeton Instruments SP-2558), with a photon counting detector (PDM series from MPD). Timing was controlled electronically using a PicoHarp300 event timer. PL decays were measured at the peak wavelengths of the PL spectra. Measurements were carried out in ambient air (21 °C) on encapsulated samples.

Transient Absorption Spectroscopy (TAS) measurements

Transient Absorption Spectroscopy (TAS) measurements were carried out using a Spectra Physics Mai Tai-Empower-Spitfire Pro Ti:Sapphire regenerative amplifier. The amplifier generates an ultra-fast laser with 35 fs pulse duration, 800 nm centre wavelength and 5 kHz repetition rate. The optical pump excitation was obtained by frequency doubling the fundamental laser output through a BBO crystal, resulting in 400 nm pulses. The white light was generated by focusing the fundamental laser pulses to 2 mm C-cut sapphire crystal window (Newlight Photonics Inc.). The white light was then focused to the centre of thin films. The fluence of the pump was set at 41 $\mu J/cm^2$ and the fluence of white light probe was much weaker than the pump, negligibly affecting the excitation population. The transmitted white light was collected by a silicon photodetector for different delays of the pump beam with the detection wavelengths tuned by the Oriel® CS130B 1/8m monochromator, mapping the white light transmission ($\Delta T/T$) as a function of time and wavelengths after photoexcitation.

Ultraviolet-Visible absorption spectrophotometry measurements

UV-Vis absorption spectra were measured by V-770 spectrophotometer (JASCO).

Atomic force microscopy (AFM)

AFM images were obtained using an AFM instrument (Park Systems XE-100) operating in non-contact mode.

Grazing-incidence wide-angle X-ray scattering (GIWAXS)

Grazing-incidence wide-angle X-ray scattering (GIWAXS) data was acquired at the XMaS beamline at the European Synchrotron Radiation Facility. To ensure structural observations were correlated

with other measurements, samples were prepared by exfoliating encapsulated samples using a second substrate and peeling the cover glass/epoxy/perovskite from the substrate. Films were measured under N_2 to avoid any ambient degradation. A 12 keV ($\lambda = 1.033$ Å) synchrotron beam was incident at 0.2° where the intensity was maximised. Scattering was collected using with a Pilatus 1M (DECTRIS) hybrid photon counting detector with a sample-to-detector distance of 280 mm, with the geometry calibrated using an LaB_6 calibrant. Detector images were resampled into Q-space and azimuthally integrated using scripts based on the PyFAI and pygix libraries.[2] Background subtraction was performed on the 2D data to minimise scattering from the epoxy encapsulant using data acquired on glass/epoxy samples (2D scattering patterns without background are given in **Figure S2**). An additional asymmetric least-squares smoothing background was subtracted from the 1D azimuthally integrated data.

Ultraviolet Photoelectron Spectroscopy (UPS)

Ultraviolet photoelectron spectra were collected using a photoelectron spectrometer (Thermo Fisher Scientific Theta Probe) with a He I (21.22 eV) ultraviolet source in Smart Lab at the Hanyang LINC + analytical center (Seoul).

Density Functional Theory (DFT) Simulations

DFT calculations were performed using the SIESTA[3,4] code based on a basis set of finite-range of numerical atomic orbitals. For structural optimization, we used the van der Waals density functional with C09 exchange[5] within the van der Waals DF2 flavour to describe the exchange-correlation term (the SIESTA version "master-post-4.1-251" was modified to include DF2 flavour). This tuning was suggested to improve C09-based geometry optimization over that with the original DF1 flavour.[6] The structures are relaxed using the fast inertial relaxation engine (FIRE) algorithm[7] until the structure satisfies the following relaxation criteria: (i) the two consecutive ionic steps have an energy difference less than 10^{-4} eV, (ii) the maximum forces acting on each atom are less than 0.02 eV Å−1(0.06 eV Å−1 for the heterostructure).

Norm-conserving Troullier-Martins pseudopotentials were used for each atomic species to account for the core electrons.[8] $1s^1$, $2s^22p^2$, $2s^22p^3$, $4s^24p^5$, and $5d^{10}6s^26p^2$ were used as valence electrons for H, C, N, Br, and Pb respectively. Polarized double-ζ (DZP) basis sets with an energy shift of 50 meV and a real space mesh grid energy cutoff of 400 Rydberg were used for the calculations. To describe accurately the properties of the surface of the CsBr terminated $CsPbBr_3$ slab, we included (5s, 5p, 5d) orbitals for Br atoms of the top two atomic layers with 30% diffuse orbital size.[9] For 3D perovskite, we used 8×6×8 and 4×4×1 Monkhorst-Pack k-point grids for the bulk and slab systems, respectively.

For 2D perovskite, we used 8×2×8 and 4×4×1 Monkhorst-Pack k-point grids for the bulk and slab systems, respectively.

For band alignments, we used single-point calculations with GGA-PBE functional as well as the Slater half-occupation technique in the so called DFT-1/2[10,11], including spin-orbit coupling (SOC) in its on-site approximation as proposed by Fernàndez-Seivane et al.[12]

Before considering slab and heterostructure calculations, we first started with the structural optimization of bulk materials. Starting with the experimental room temperature structures of orthorhombic $CsPbBr_3$ and $BA_2CsPb_2Br_7$[13–15], unit cell parameters as well as internal atomic positions were allowed to relax (Table S4). Then, to compute the energies at the top of the valence band (ionization energy) of bulk materials, we constructed slabs from these optimized structures. For $CsPbBr_3$ we considered a 10 octahedra thick slab with the 6 inner octahedra kept frozen to mimic the bulk region. Atomic positions of the two outer-layers were allowed to relax. For $BA_2CsPb_2Br_7$, we extracted three distinct n=2 layers and allowed relaxation of the atomic positions of the two outer layers. For the construction of the 2D/3D heterostructure, we started from the optimized $CsPbBr_3$ bulk, averaged the in-plane parameters to $a'=c'=\sqrt{(ac)}$ and re-optimized the b parameter and internal atomic positions. Then, we constructed the 3D section of the heterostructure by cutting a slab of 9 octahedra along the b' axis. Finally, the optimized 2D structure was lattice matched with this slab, imposing identical in-plane parameters. The 2D section is made of two distinct n=2 layers. To mimic the 3D bulk part in the model heterostructure, the 5 internal octahedra layers of the 3D section were kept frozen, whereas the top two octahedra layers of the 3D section as well as the 2D sections were allowed to relax. We stress that the in-plane lattice constants of the 3D part were imposed for the whole heterostructure and were not allowed to relax during the 2D/3D interface structural optimization. We only allowed the out-of-plane lattice constant to relax along with the atomic positions. This strategy allows to capture the interface effects during the relaxation while maintaining the integrity of the bulk region of heterostructures, which is useful for the energy level alignment.

The absolute energies at the top of the valence band of the slabs (**Figure S22**) and their relative position in the heterostructure (**Figure S21**) were computed using the method known as Hartree potential alignment, using the protocols described in ref [9,11]and [16,17], respectively.

$(BABr)_x(CsPbBr_3)_{1-x}$	**x=0.17 (mg/ml)**	**x=0.31 (mg/ml)**	**x=0.42 (mg/ml)**	**x=0.5 (mg/ml)**	**x=0.58 (mg/ml)**
$PbBr_2$	63.344	59.808	56.28	52.744	49.208
CsBr	36.784	34.76	32.744	30.72	28.704
BABr	5.616	11.232	16.856	22.472	28.088
18-crown-6	4	4	4	4	4

Table S1 – Exact masses required for perovskite precursor solution per 1ml of DMSO.

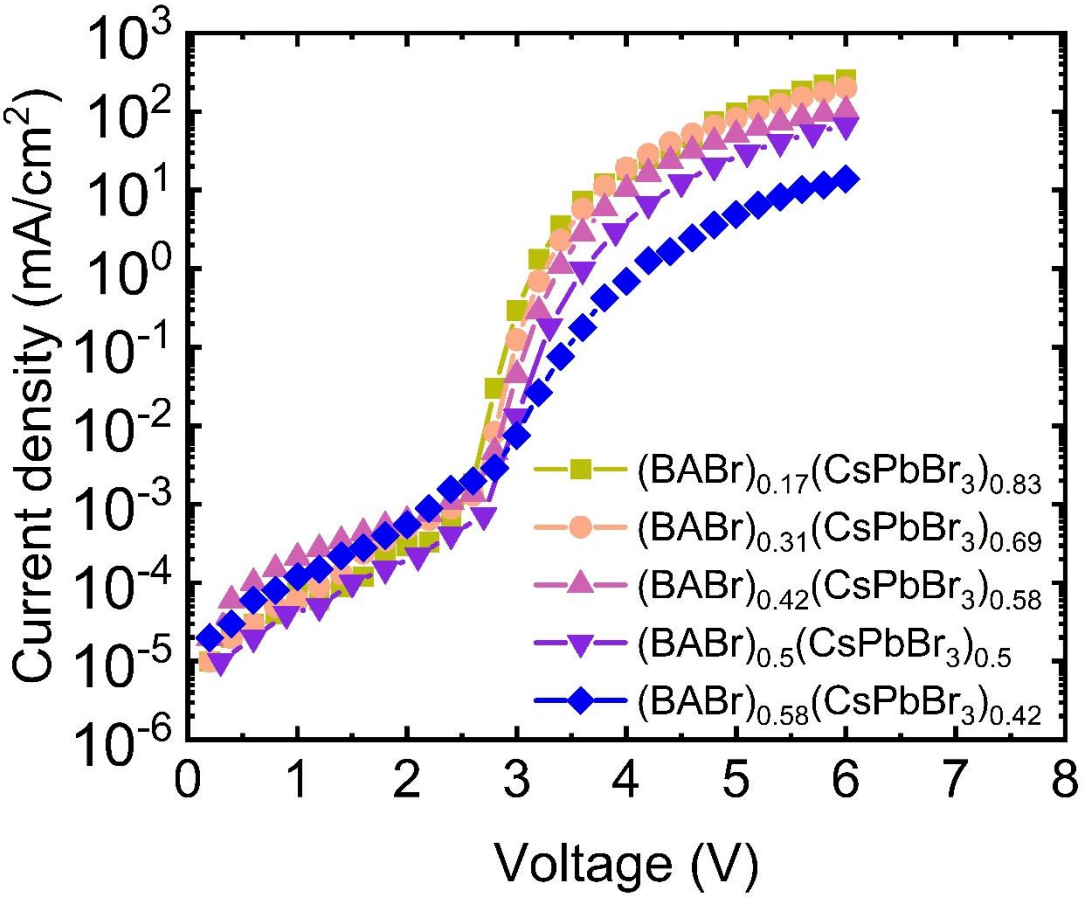

Figure S1. Current density – Voltage characteristics for representative LEDs employing $(BABr)_x(CsPbBr_3)_{1-x}$ as the perovskite emitting layer.

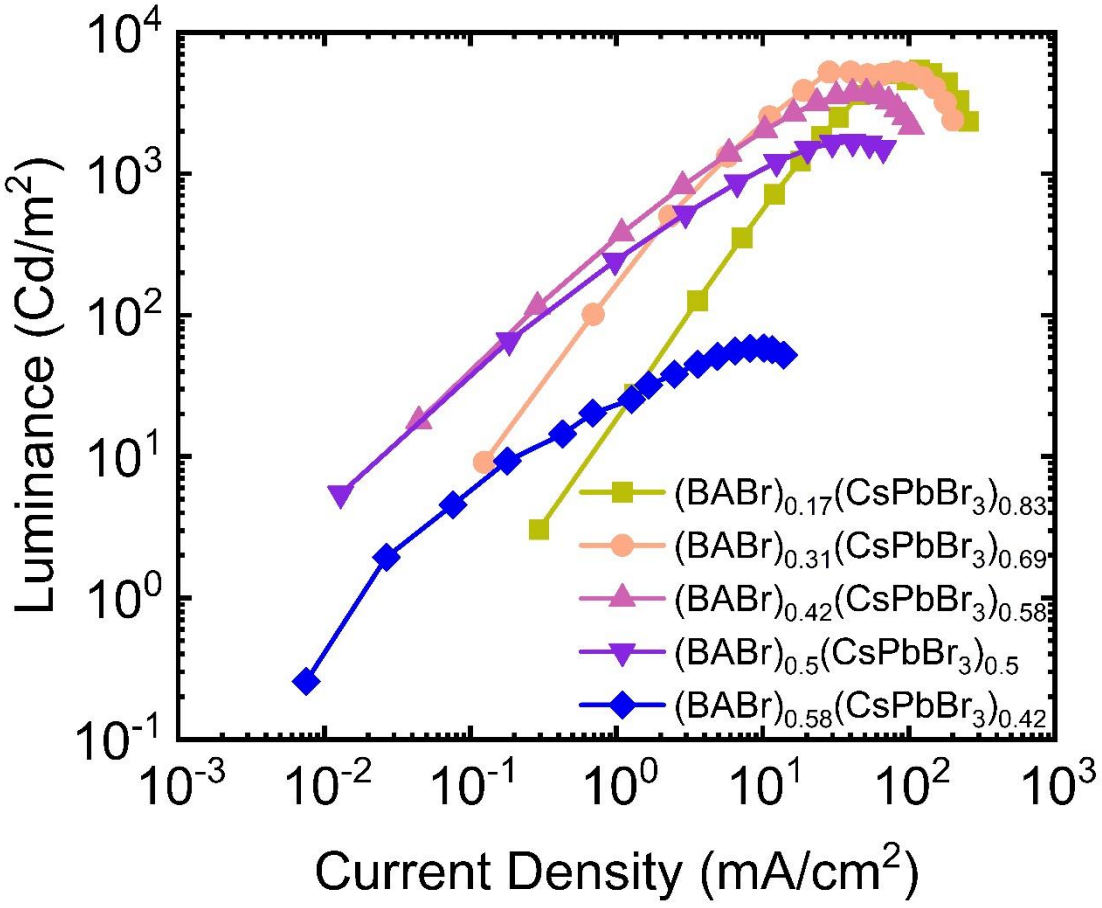

Figure S2 – Luminance - Current density characteristics for representative LEDs employing $(BABr)_x(CsPbBr_3)_{1-x}$ as the perovskite emitting layer.

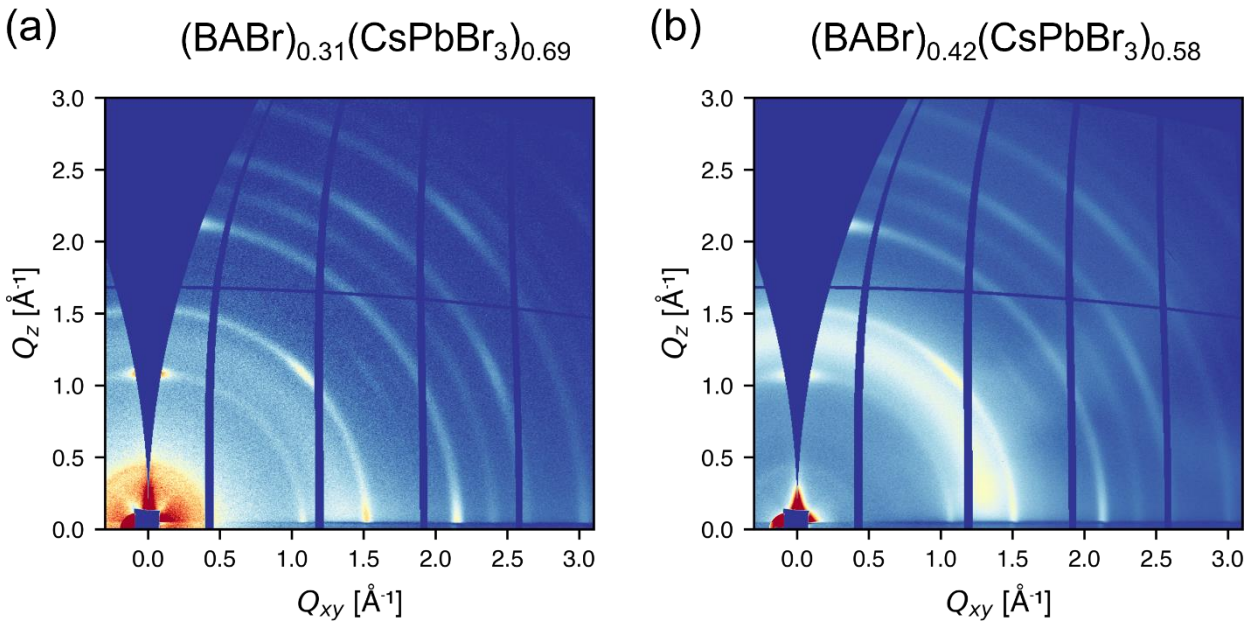

Figure S3: 2D GIWAXS patterns from a) $(BABr)_{0.31}(CsPbBr_3)_{0.69}$ and b) $(BABr)_{0.42}(CsPbBr_3)_{0.58}$ films. The Debye-Scherrer ring at Q ~0.4 $Å^{-1}$ and broad ring at Q ~1.3 $Å^{-1}$ are backgrounds from a polyimide window and epoxy substrate remaining after the background subtraction.

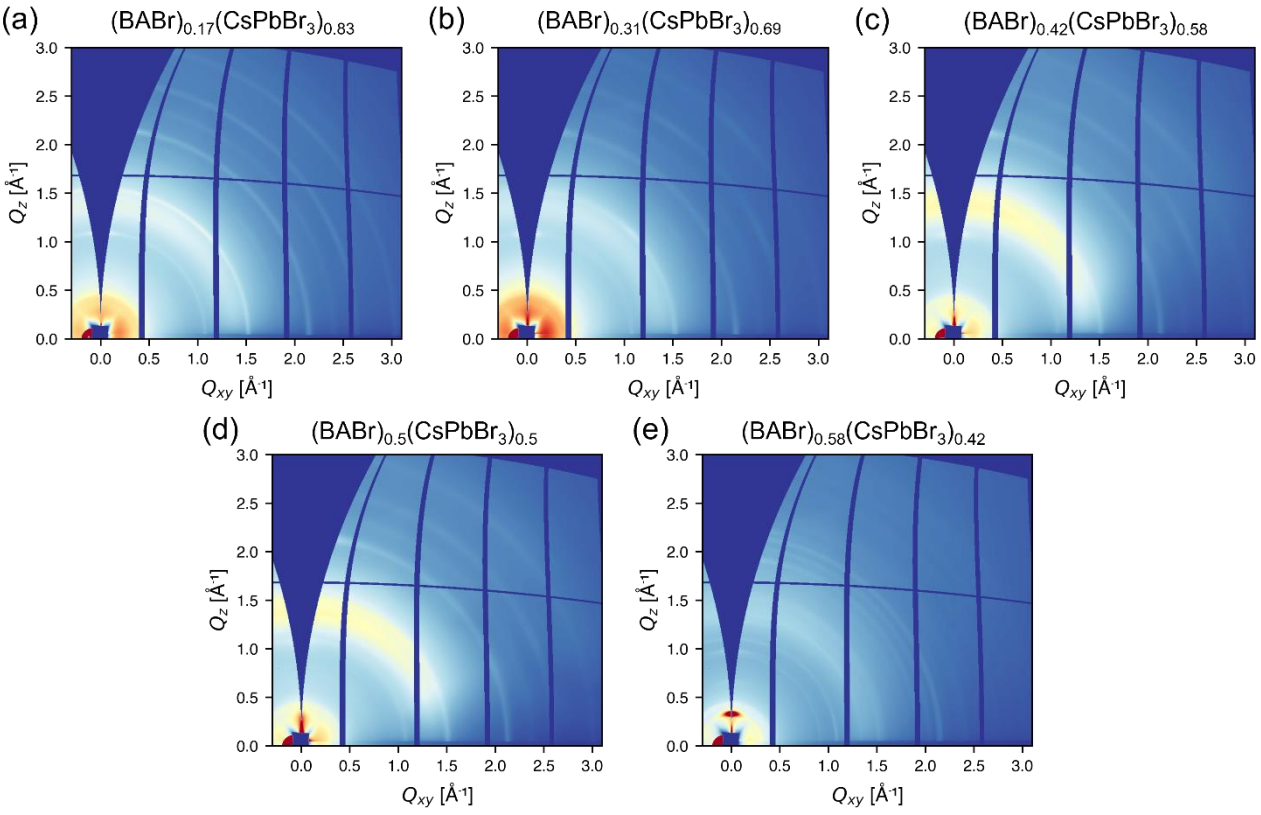

Figure S4: 2D GIWAXS patterns prior to epoxy background subtraction from a) $(BABr)_{0.17}(CsPbBr_3)_{0.83}$, b) $(BABr)_{0.31}(CsPbBr_3)_{0.69}$, c) $(BABr)_{0.42}(CsPbBr_3)_{0.58}$, d) $(BABr)_{0.5}(CsPbBr_3)_{0.5}$ and e) $(BABr)_{0.58}(CsPbBr_3)_{0.42}$.

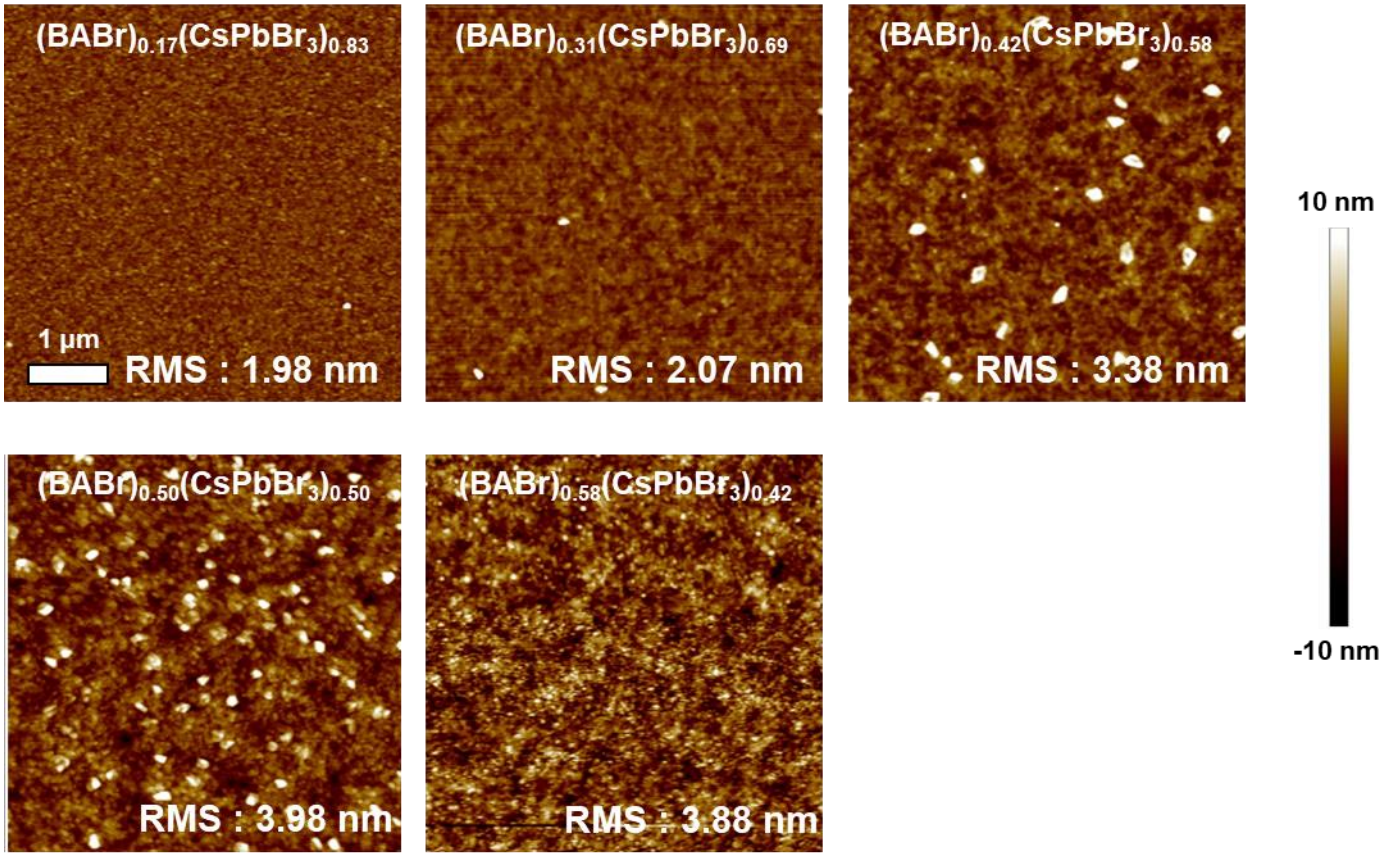

Figure S5. Atomic force microscopy (AFM) images of $(BABr)_x(CsPbBr_3)_{1-x}$ thin films deposited on glass.

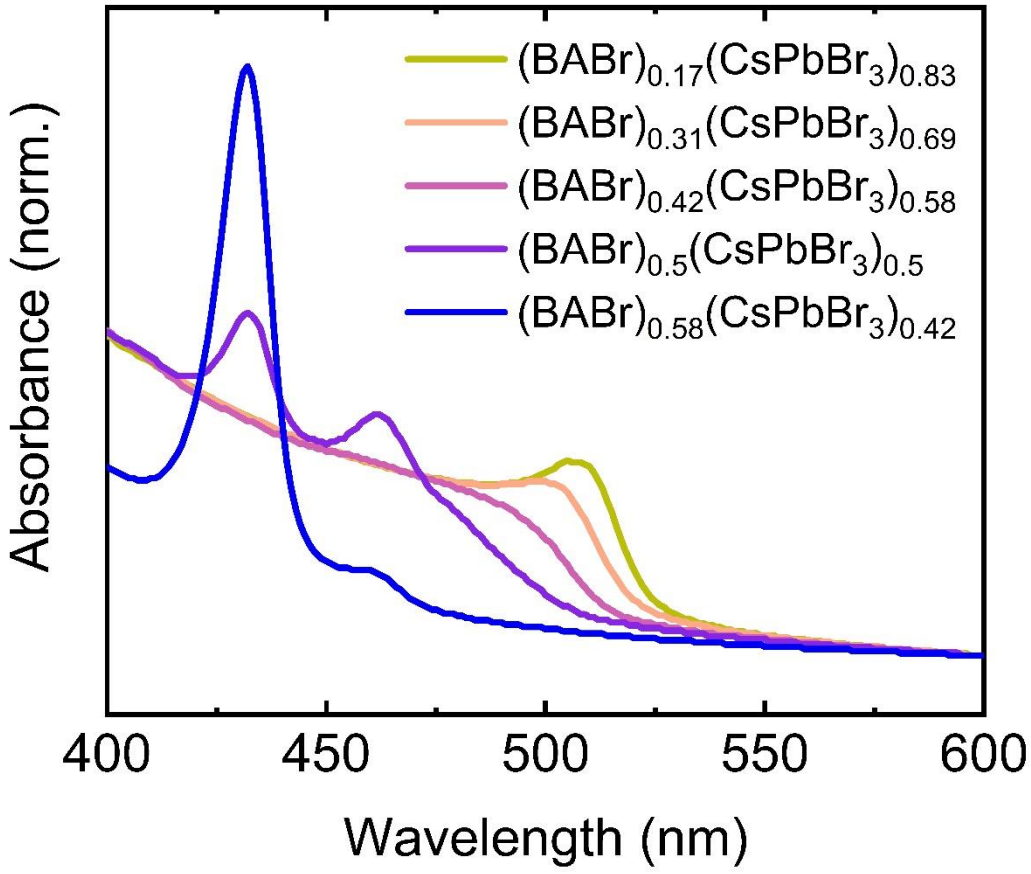

Figure S6 – Absorbance spectra of thin films of $(BABr)_x(CsPbBr_3)_{1-x}$ deposited on glass.

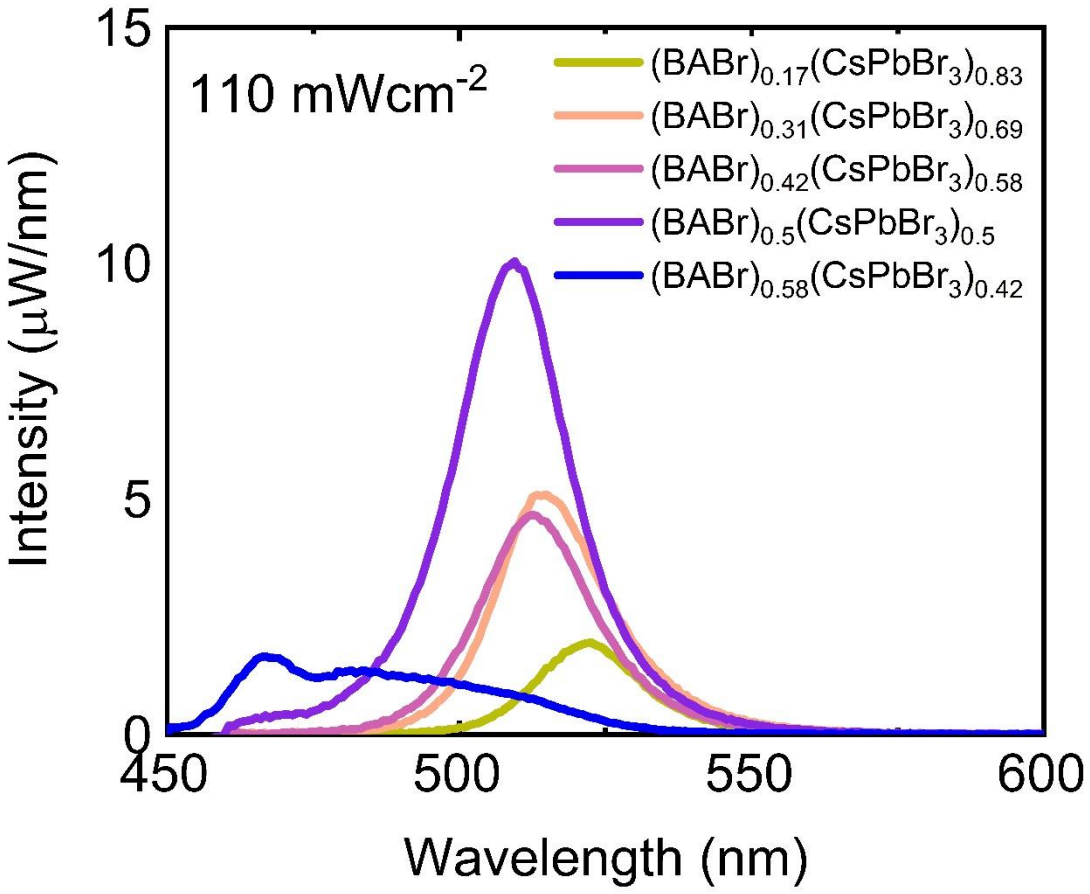

Figure S7 – Photoluminescence spectra of thin films of $(BABr)_x(CsPbBr_3)_{1-x}$ deposited on glass.

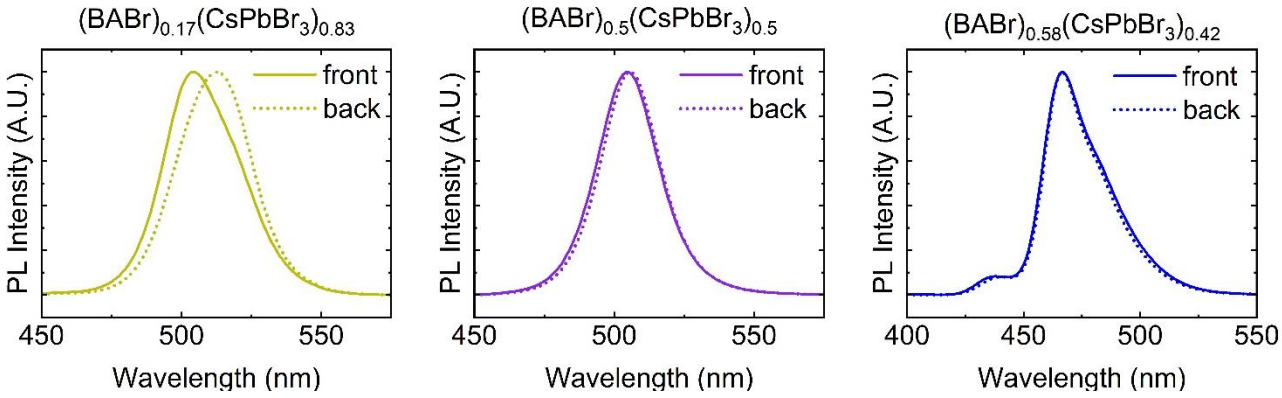

Figure S8 – Normalised photoluminescence spectra of thin films of 3 compositions of $(BABr)_x(CsPbBr_3)_{1-x}$ deposited on glass measured with laser excitation from the front and back side of the sample.

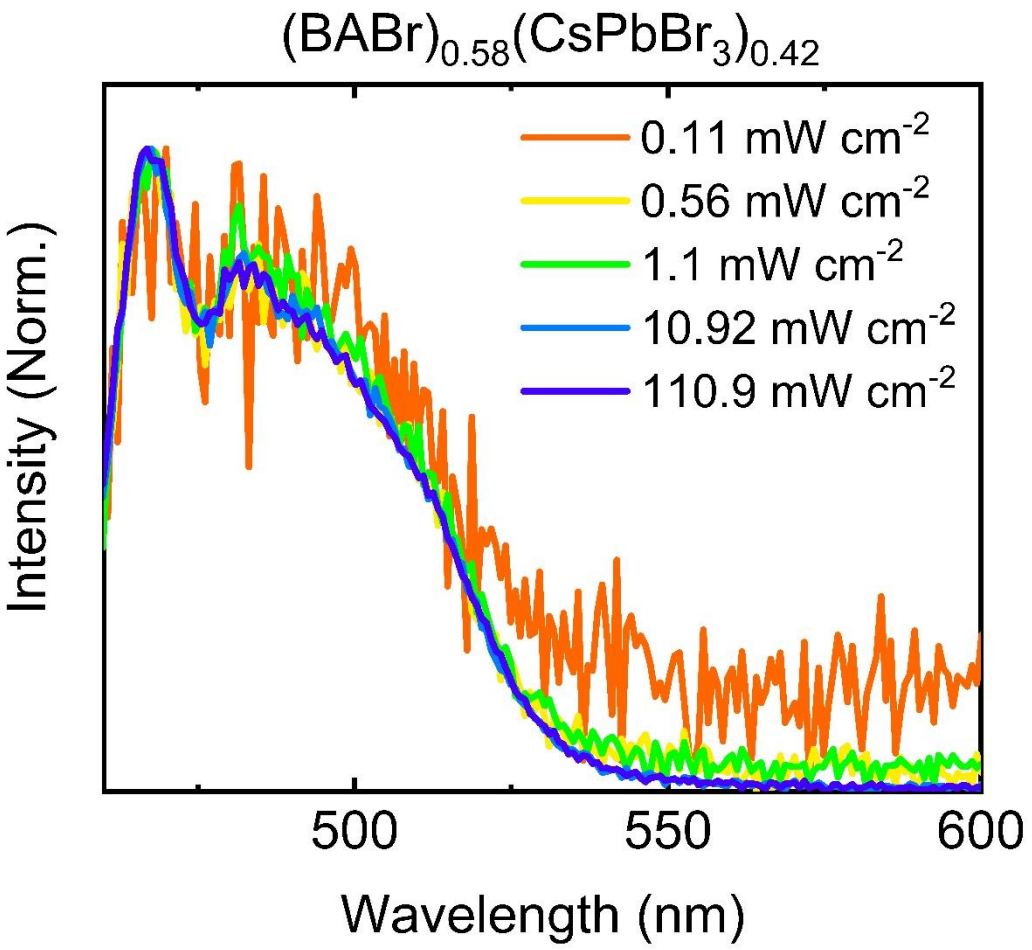

Figure S9 – Normalised photoluminescence spectra of thin films of $(BABr)_{0.58}(CsPbBr_3)_{0.42}$ deposited on glass with increasing laser intensity demonstrating that there is no change to the photoluminescence character with increasing intensity of excitation.

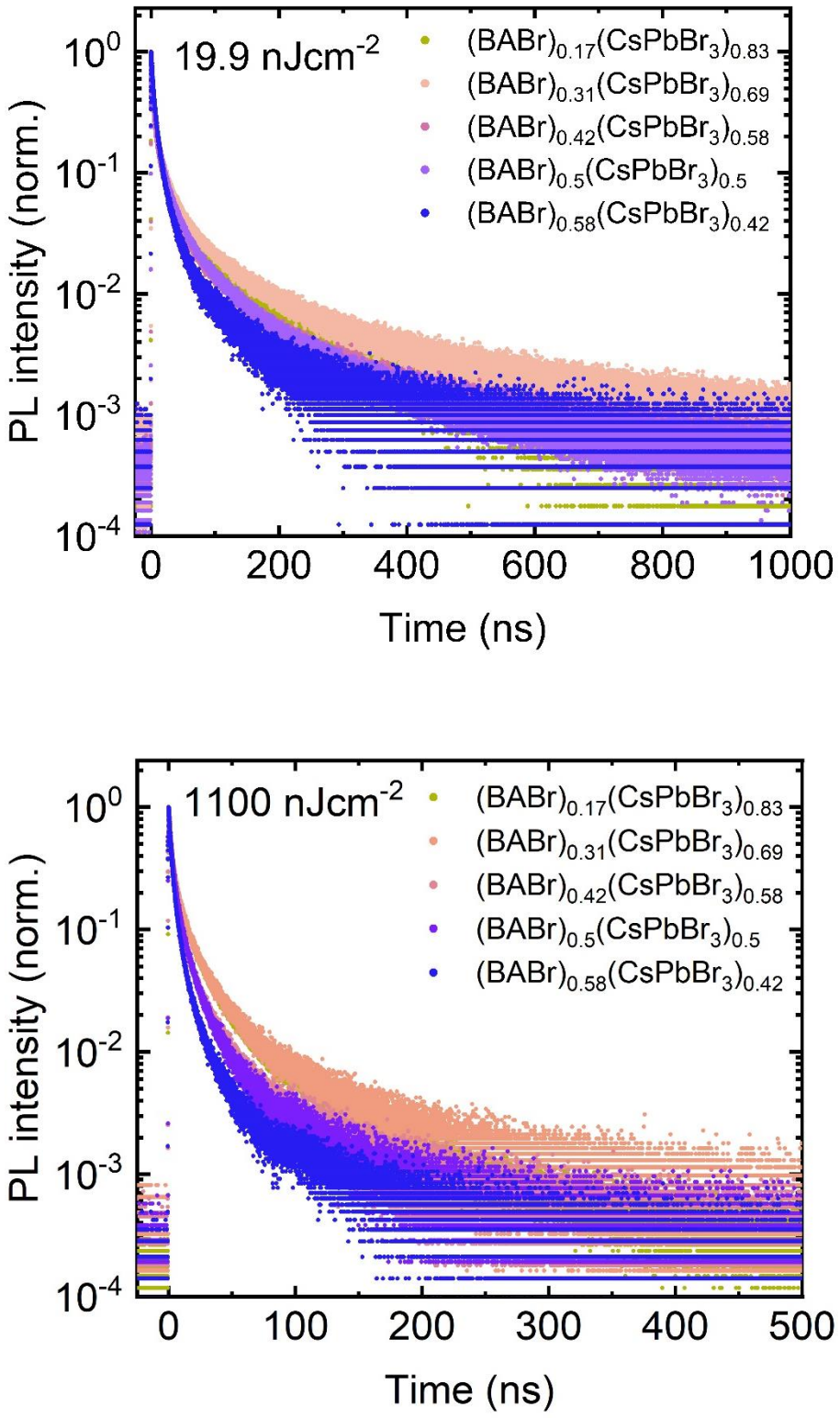

Figure S10 – Time-correlated single photon counting (TCSPC) measurements, excited at 400 nm laser fluence in plot of thin films of $(BABr)_x(CsPbBr_3)_{1-x}$ deposited on glass.

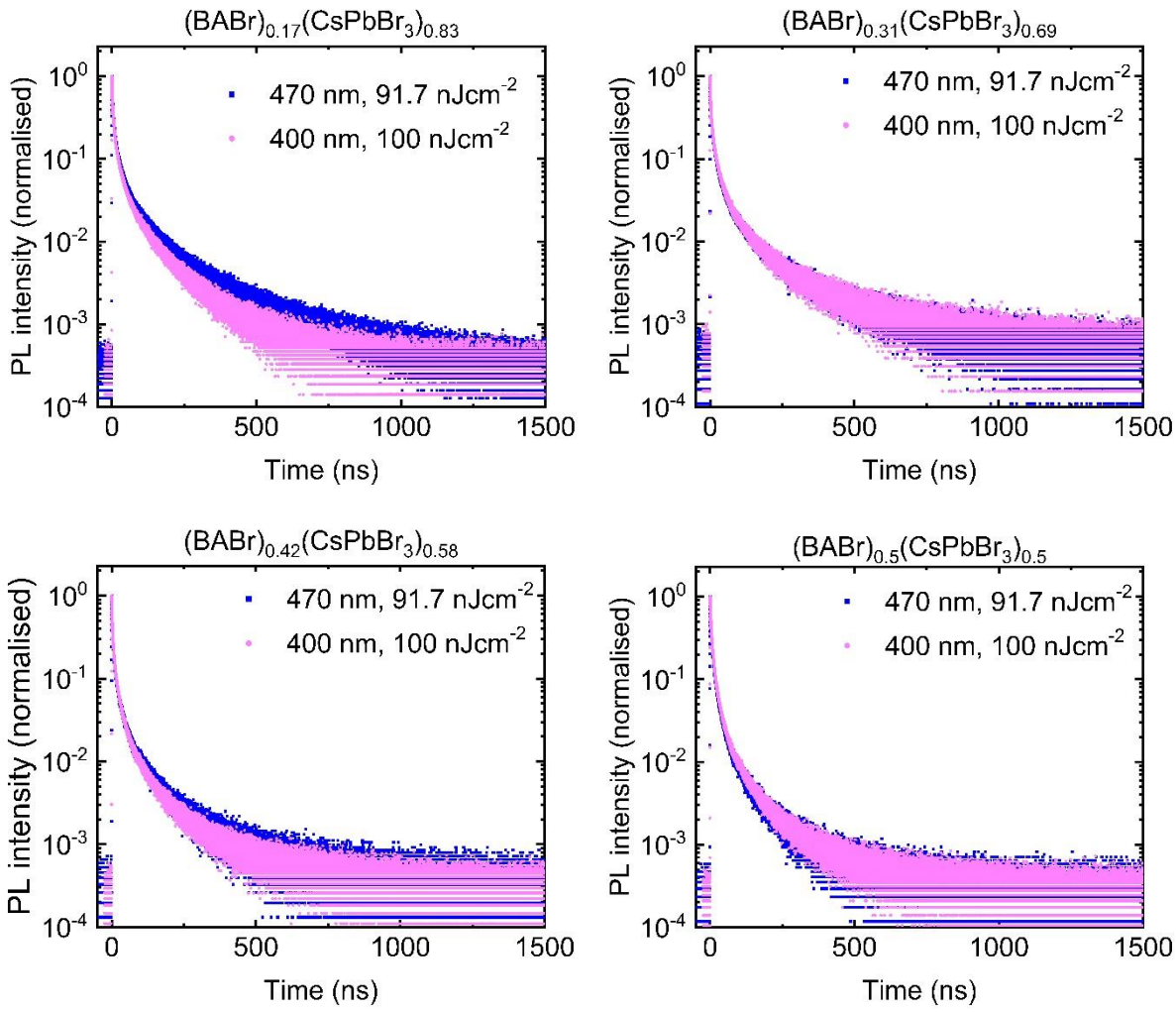

Figure S11 – Comparison of time-correlated single photon counting (TCSPC) measurements of thin films of $(BABr)_x(CsPbBr_3)_{1-x}$ deposited on glass excited at 400 and 470 nm with similar laser fluence.

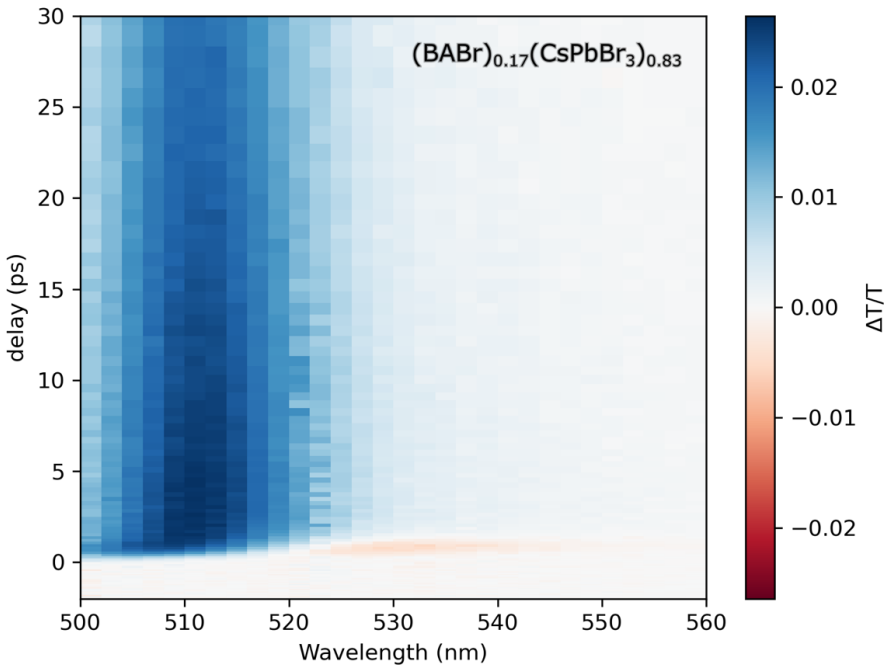

Figure S12 - 2D colour map of the transient absorption signal (ΔT/T) as a function of delay and wavelength for a $(BABr)_{0.17}(CsPbBr_3)_{0.83}$ thin film excited at a wavelength of 400 nm with a pulse fluence of 41 µJ/cm^2.

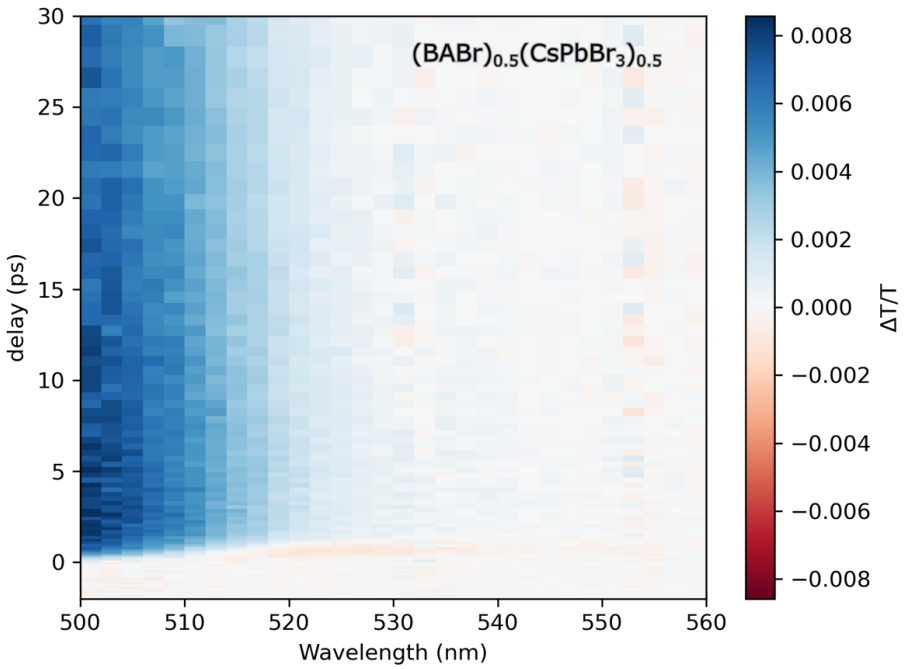

Figure S13 - 2D colour map of the transient absorption signal (ΔT/T) as a function of delay and wavelength for a $(BABr)_{0.5}(CsPbBr_3)_{0.5}$ thin film excited at a wavelength of 400 nm with a pulse fluence of 41 µJ/cm^2.

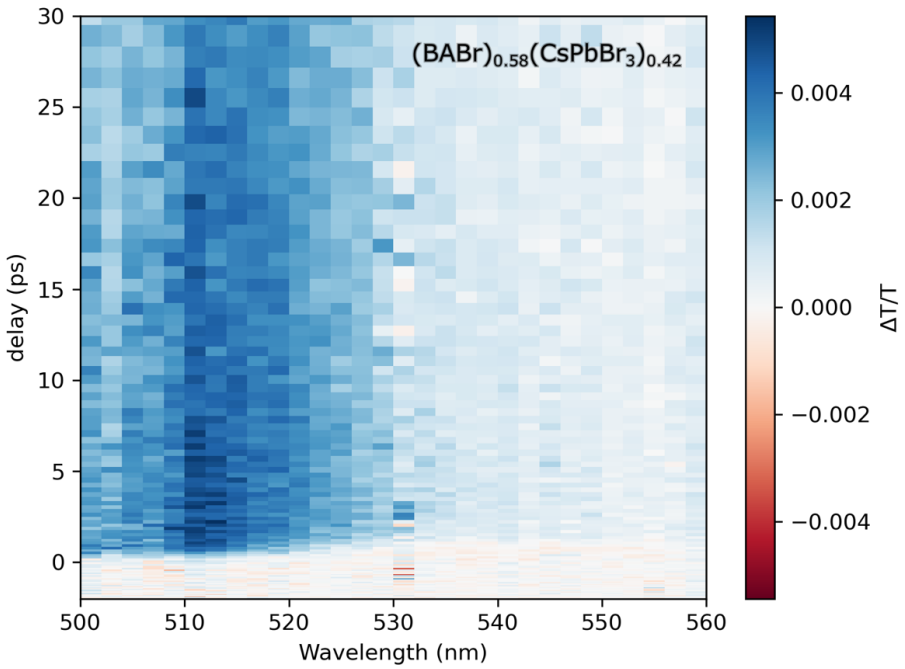

Figure S14 - 2D colour map of the transient absorption signal (ΔT/T) as a function of delay and wavelength for a $(BABr)_{0.58}(CsPbBr_3)_{0.42}$ thin film excited at a wavelength of 400 nm with a pulse fluence of 41 µJ/cm^2.

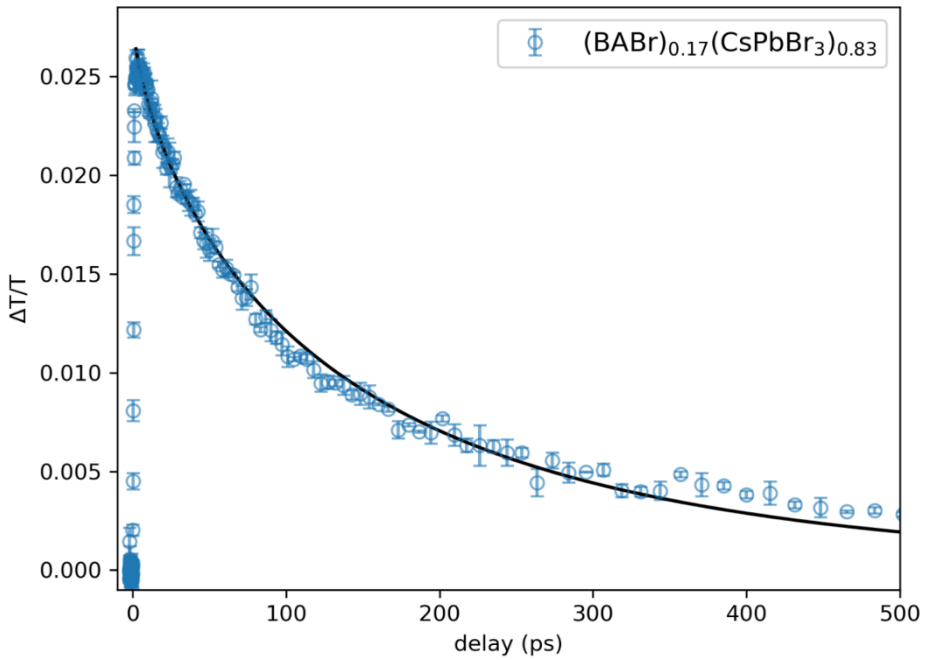

Figure S15 - Transient absorption decay (ΔT/T) recorded for a probe wavelength of 510 nm for the $(BABr)_{0.17}(CsPbBr_3)_{0.83}$ thin film with a 400 nm pump excitation at a fluence of 41 µJ/cm^2. The solid line is a fit to the data based on a stretched exponential.

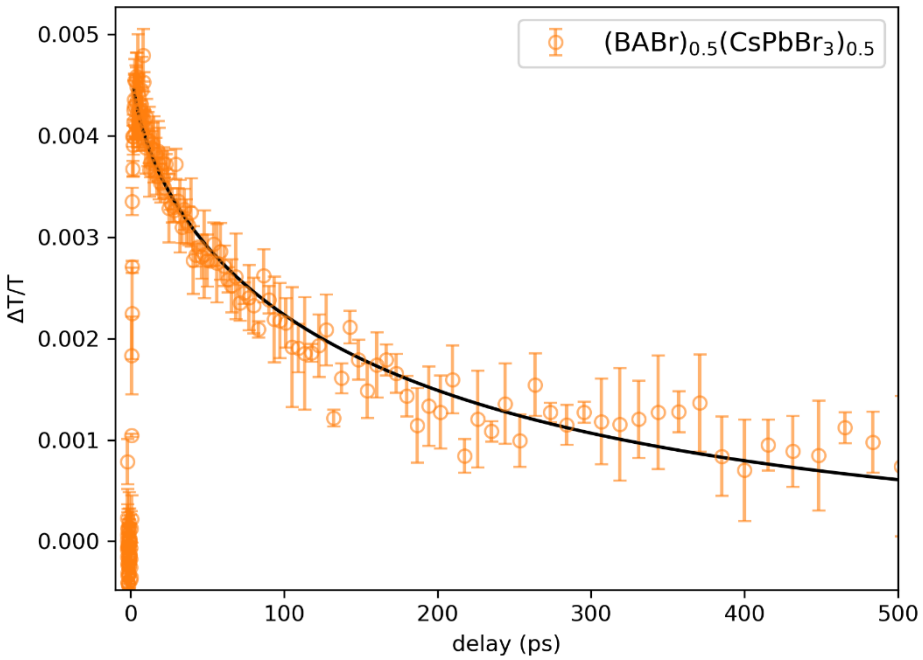

Figure S16 - Transient absorption decay (ΔT/T) recorded for a probe wavelength of 510 nm for the $(BABr)_{0.5}(CsPbBr_3)_{0.5}$ thin film with a 400 nm pump excitation at a fluence of 41 μJ/cm^2. The solid line is a fit to the data based on a stretched exponential.

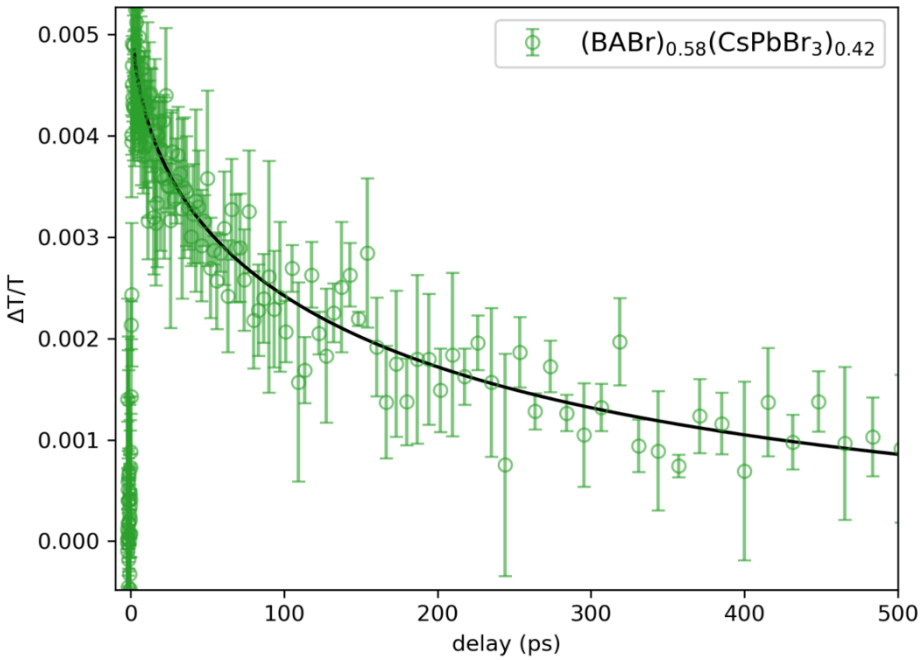

Figure S17 - Transient absorption decay (ΔT/T) recorded for a probe wavelength of 510 nm for the $(BABr)_{0.58}(CsPbBr3)_{0.42}$ thin film with a 400 nm pump excitation at a fluence of 41 μJ/cm^2. The solid line is a fit to the data based on a stretched exponential.

	***τ* (ps)**	***A***	***β***
$(BABr)_{0.17}(CsPbBr3)_{0.83}$	132 ± 2	0.0272 ± 0.0002	0.73 ± 0.02
$(BABr)_{0.5}(CsPbBr3)_{0.5}$	162 ± 8	0.0046 ± 0.0001	0.63 ± 0.04
$(BABr)_{0.58}(CsPbBr3)_{0.42}$	164 ± 13	0.0052 ± 0.0002	0.53 ±0.04

Table S2 – Variables extracted from stretched exponential fits to the transient absorption decays at 510 nm for each film composition.

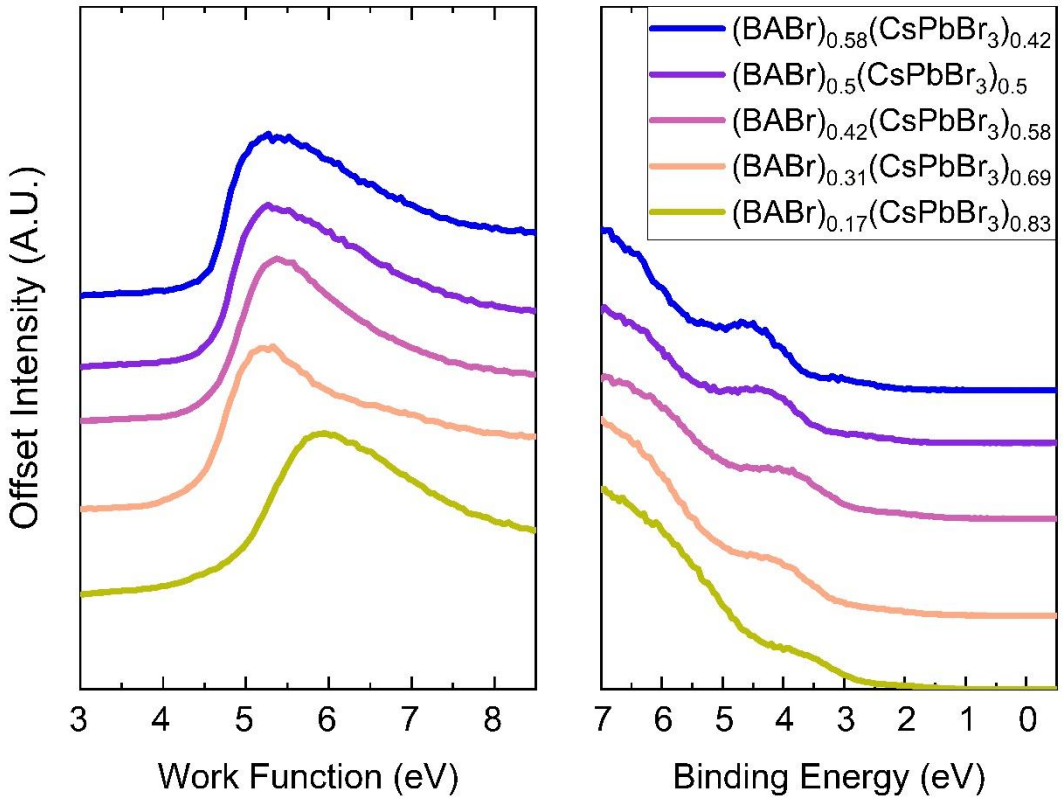

Figure S18 – Ultraviolet photoelectron spectroscopy measurements showing the secondary electron cut-off (work function) and valence band region of thin films $(BABr)_x(CsPbBr_3)_{1-x}$ deposited on ITO glass.

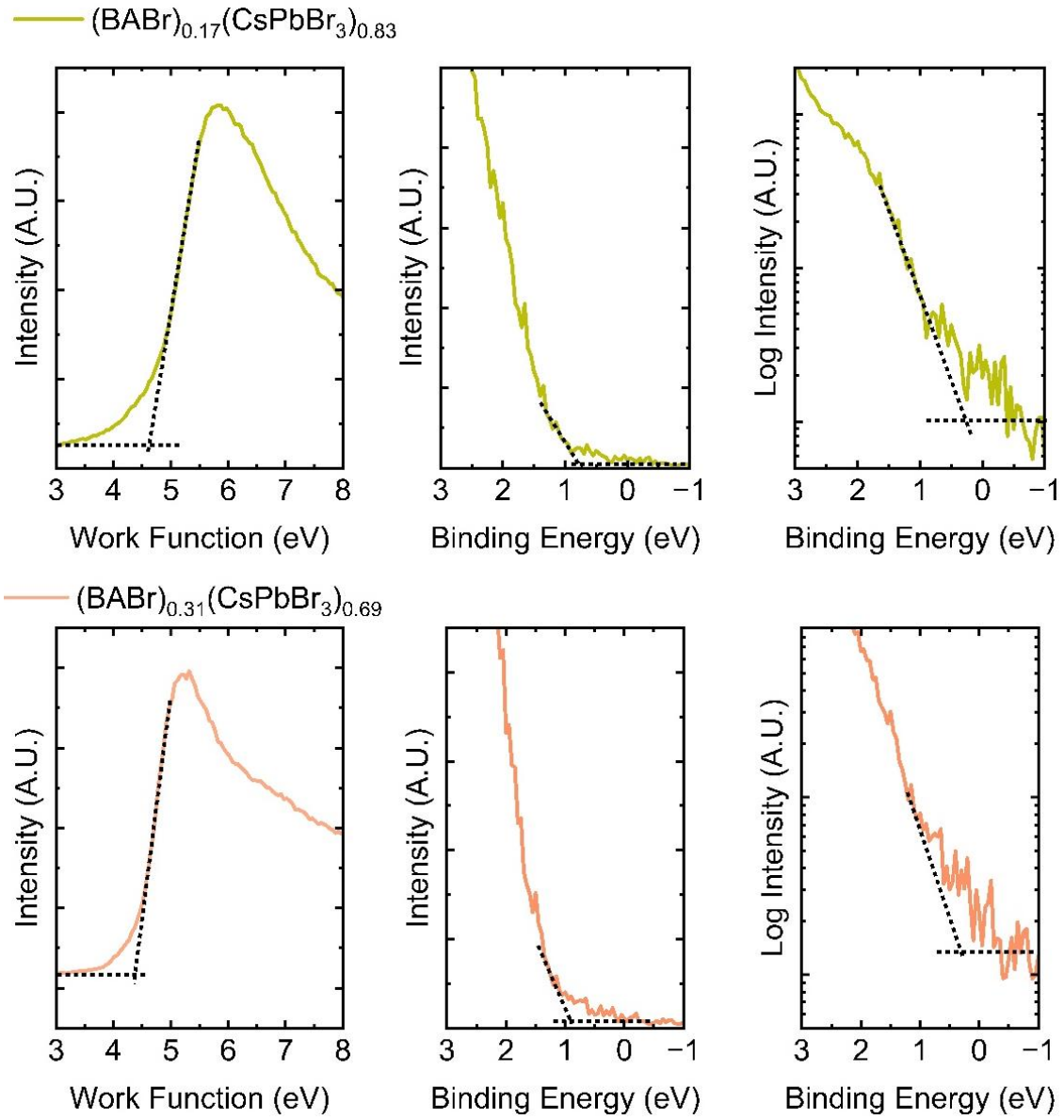

Figure S19 – Ultraviolet photoelectron spectroscopy measurements, showing fitting of secondary electron cut-off and valence band regions of thin films $(BABr)_x(CsPbBr_3)_{1-x}$ deposited on ITO glass. The valence band region has been fit using both a linear and logarithmic fitting approach.

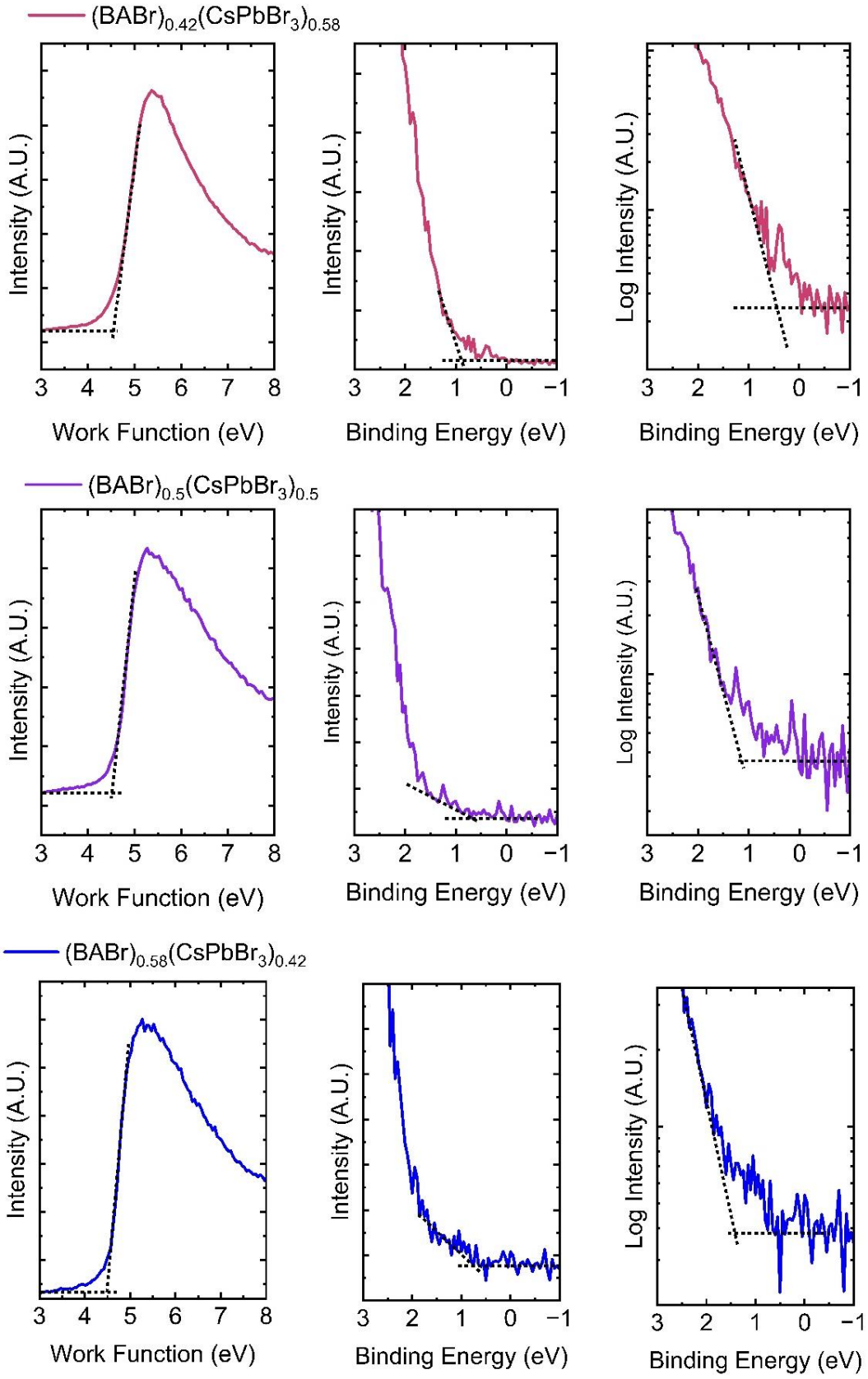

Figure S20 – Ultraviolet photoelectron spectroscopy measurements, showing fitting of secondary electron cut-off and valence band regions of thin films $(BABr)_x(CsPbBr_3)_{1-x}$ deposited on ITO glass. The valence band region has been fit using both a linear and logarithmic fitting approach.

	Work Function (eV)	Valence Band Onset – linear (eV)	Valence Band Onset – log (eV)	Valence Band Max.- linear (eV)	Valence Band Max. – log(eV)
$(BABr)_{0.17}(CsPbBr_3)_{0.83}$	-4.64	-0.79	-0.32	-5.75	-4.96
$(BABr)_{0.31}(CsPbBr_3)_{0.69}$	-4.48	-0.9	-0.43	-5.81	-4.91
$(BABr)_{0.42}(CsPbBr_3)_{0.58}$	-4.6	-0.9	-0.33	-5.83	-4.93
$(BABr)_{0.5}(CsPbBr_3)_{0.5}$	-4.57	-0.59	-1.1	-6.26	-5.67
$(BABr)_{0.58}(CsPbBr_3)_{0.42}$	-4.54	-0.58	-1.41	-6.53	-5.95

Table S3 – Energy levels of thin films $(BABr)_x(CsPbBr_3)_{1-x}$ deposited on ITO glass determined from linear and logarithmic fitting of ultraviolet photoelectron spectroscopy measurements.

	Work Function (eV)	Valence Band Onset – linear (eV)	Valence Band Onset – log (eV)	Valence Band Max.- linear (eV)	Valence Band Max. – log(eV)
$CsPbBr_3$	-4.2	-1.2	-1.06	-5.4	-5.26
$CsPbBr_3$ w/18-crown-6	-4.2	-1.14	-0.84	-5.34	-5.04
BA_2PbBr_4	-4.2	-1.37	-1.01	-5.57	-5.21
BA_2PbBr_4 w/18-crown-6	-4.3	-1.37	-1.14	-5.67	-5.44

$BA_2CsPb_2Br_7$	-3.8	-1.69	-1.47	-5.49	-5.27
$BA_2CsPb_2Br_7$ w/18-crown-6	-3.9	-1.56	-1.29	-5.46	-5.19

Table S4 – Energy levels of thin films $CsPbBr_3$, BA_2PbBr_4 and $BA_2CsPb_2Br_7$ deposited on ITO glass (with and without 18-crown-6) determined from linear and logarithmic fitting of ultraviolet photoelectron spectroscopy measurements.

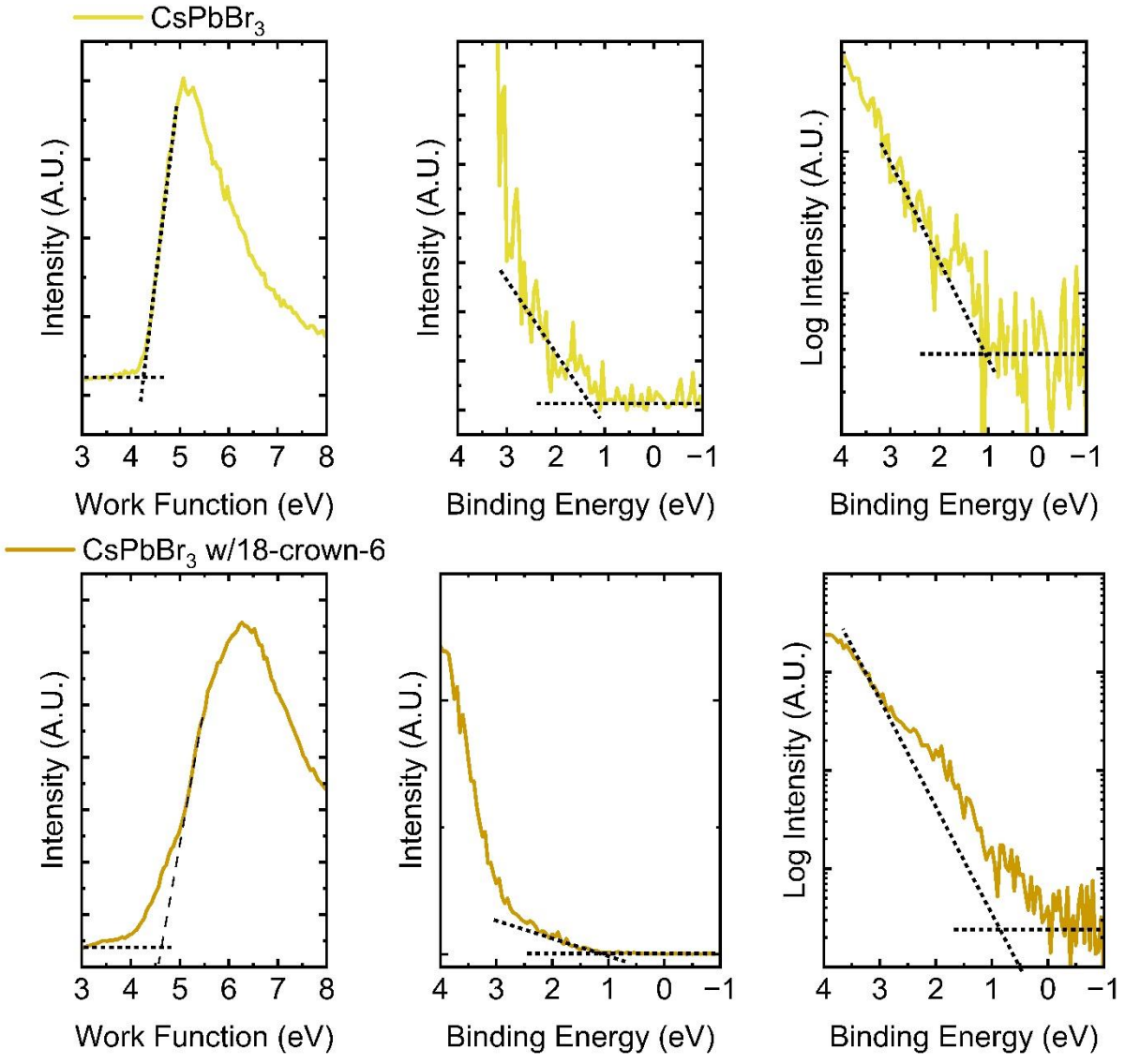

Figure S21 – Ultraviolet photoelectron spectroscopy measurements of thin films of $CsPbBr_3$ deposited on ITO glass, showing fitting of secondary electron cut-off and valence band regions. The valence band region has been fit using both a linear and logarithmic fitting approach.

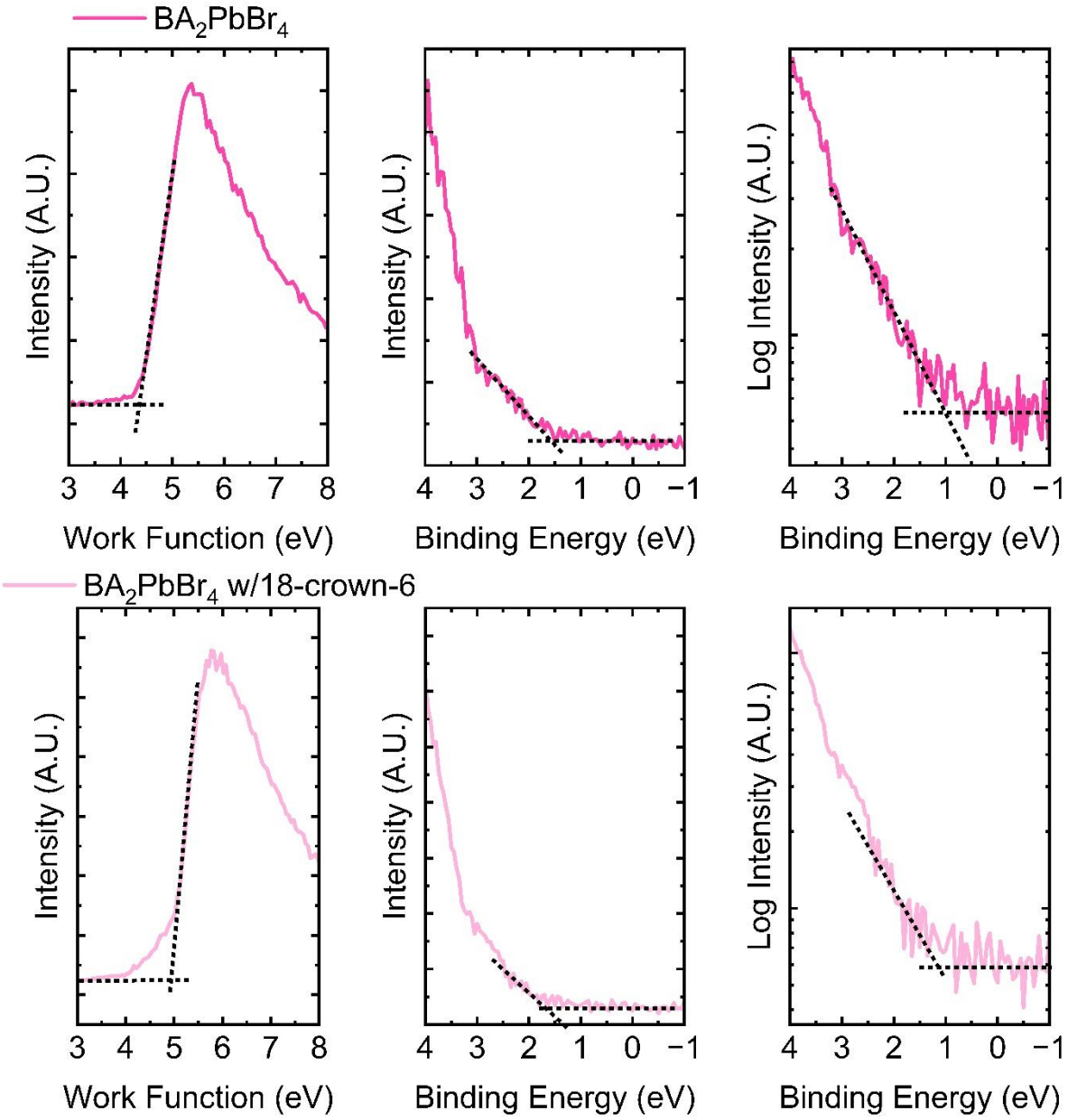

Figure S22 – Ultraviolet photoelectron spectroscopy measurements of thin films of BA_2PbBr_4 deposited on ITO glass, showing fitting of secondary electron cut-off and valence band regions. The valence band region has been fit using both a linear and logarithmic fitting approach.

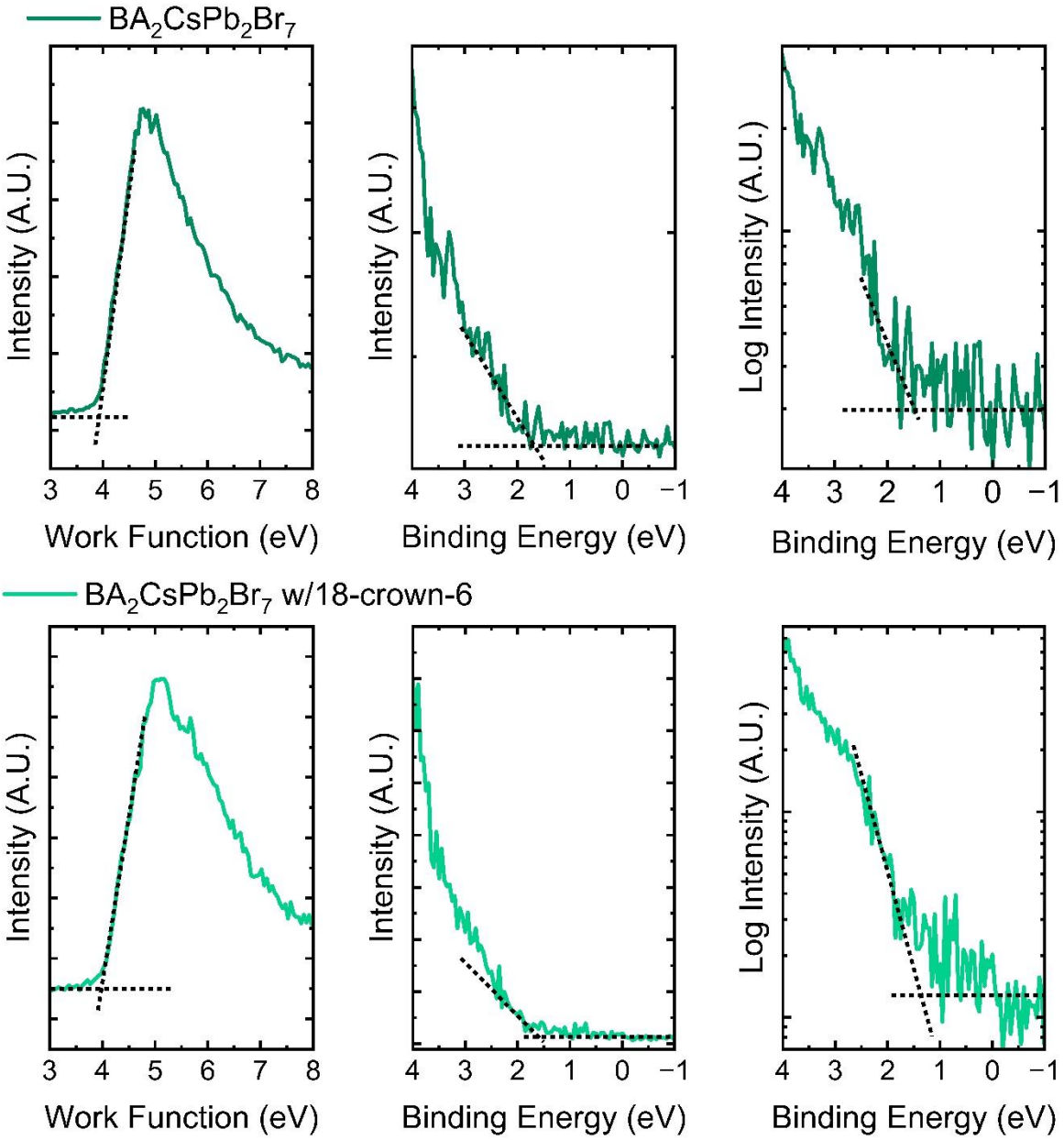

Figure S23 – Ultraviolet photoelectron spectroscopy measurements of thin films of $BA_2CsPb_2Br_7$ deposited on ITO glass, showing fitting of secondary electron cut-off and valence band regions. The valence band region has been fit using both a linear and logarithmic fitting approach.

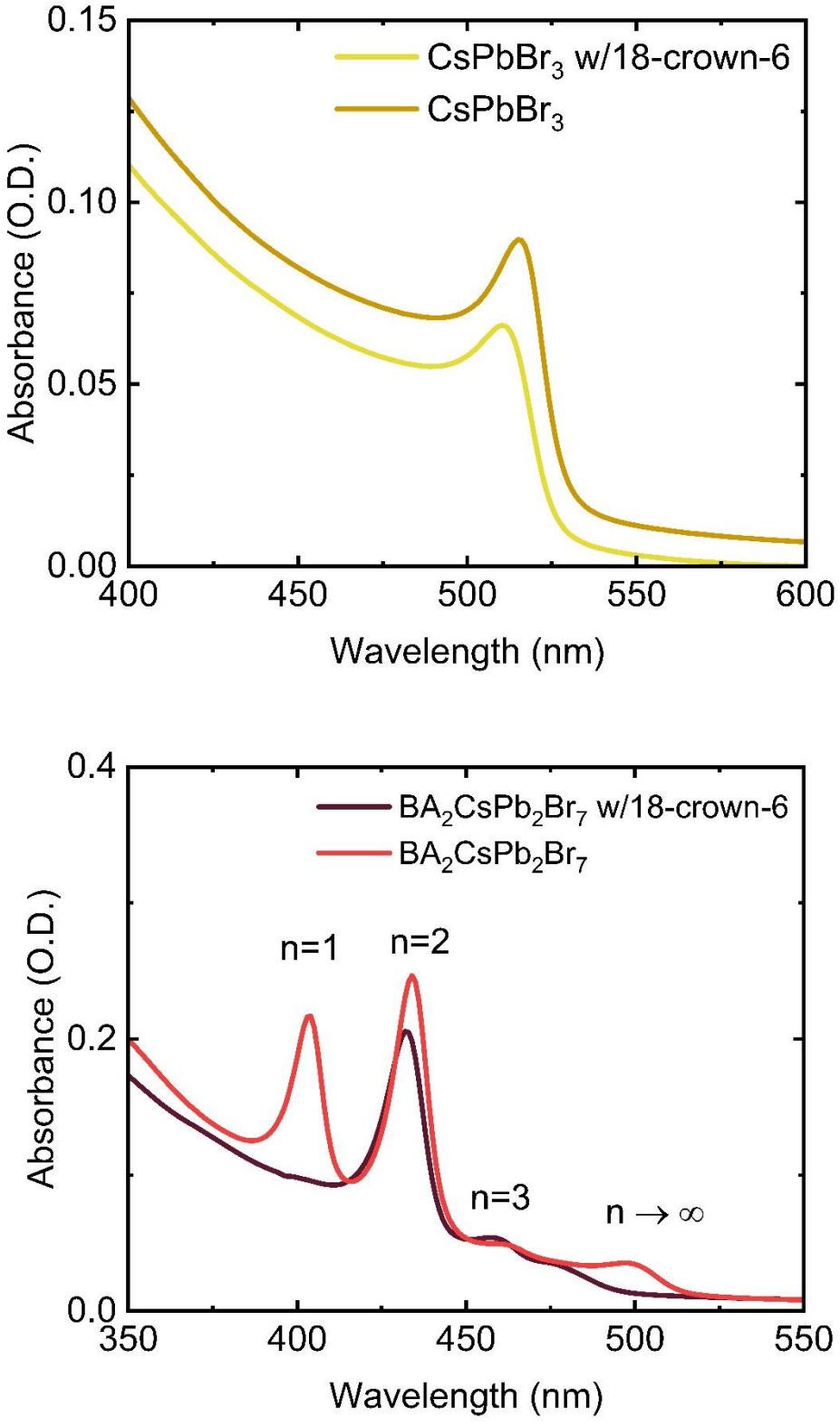

Figure S24 – Absorbance of thin films of $CsPbBr_3$ and $BA_2CsPb_2Br_7$ on glass.

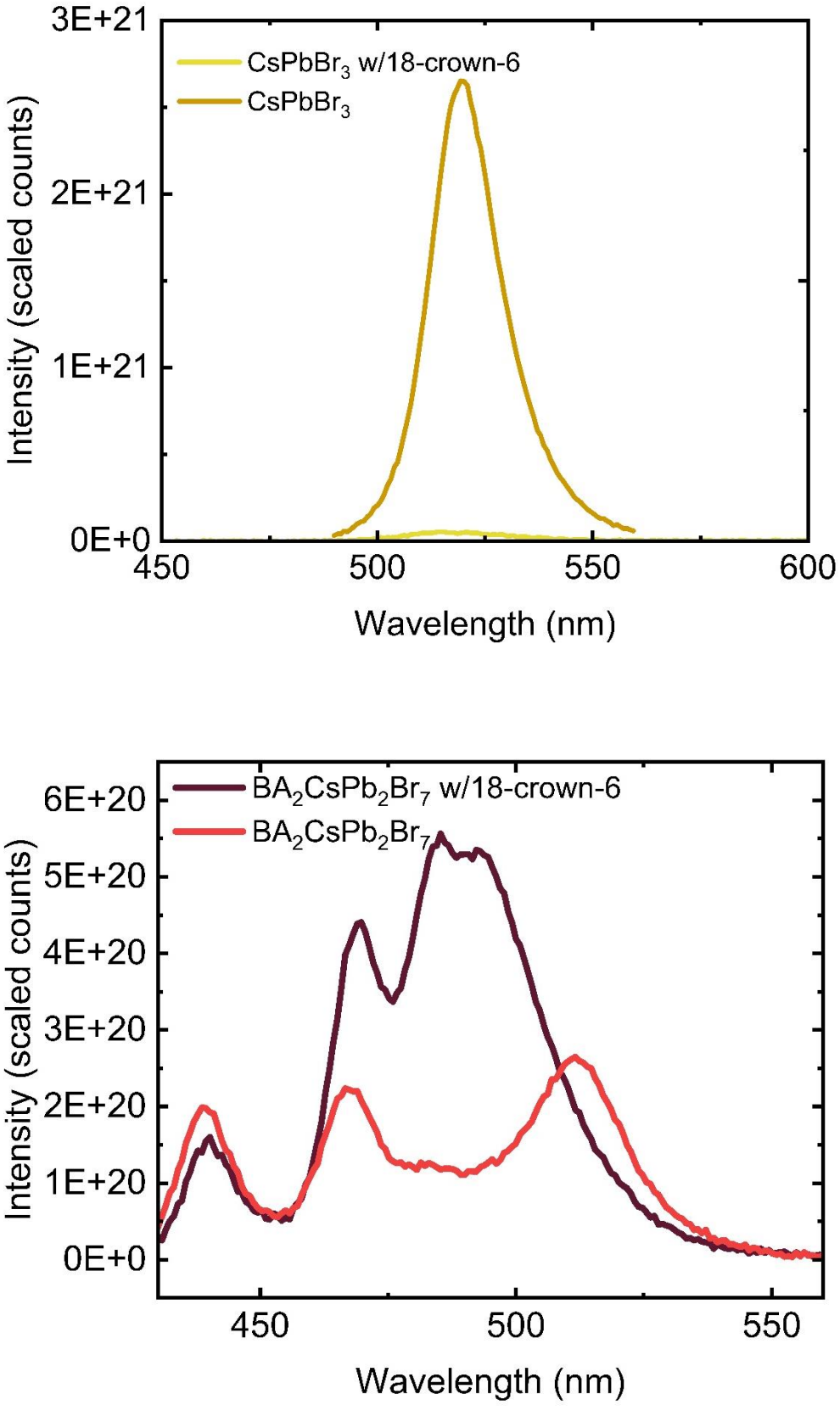

Figure S25 – Photoluminescence spectra of thin films of $CsPbBr_3$ and $BA_2CsPb_2Br_7$ on glass.

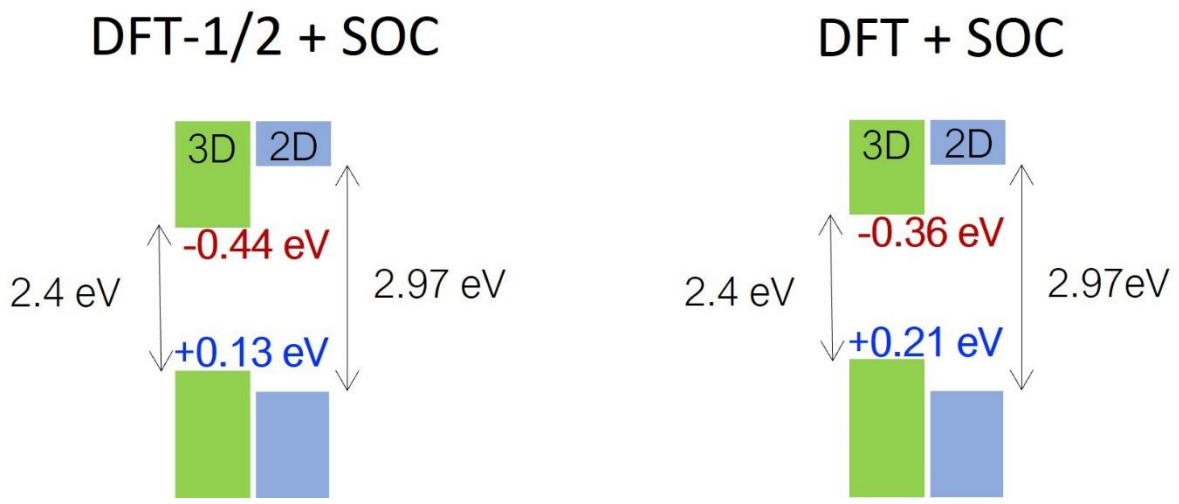

Figure S26 - Plot showing predicted energy level alignments obtained for the CsPbBr3/ $BA_2CsPb_2Br_7$ 3D/2D model heterostructure, calculated using single-point calculations with DFT-1/2 (left) and GGA-PBE (right), including spin-orbit coupling, and using experimental optical band gaps.

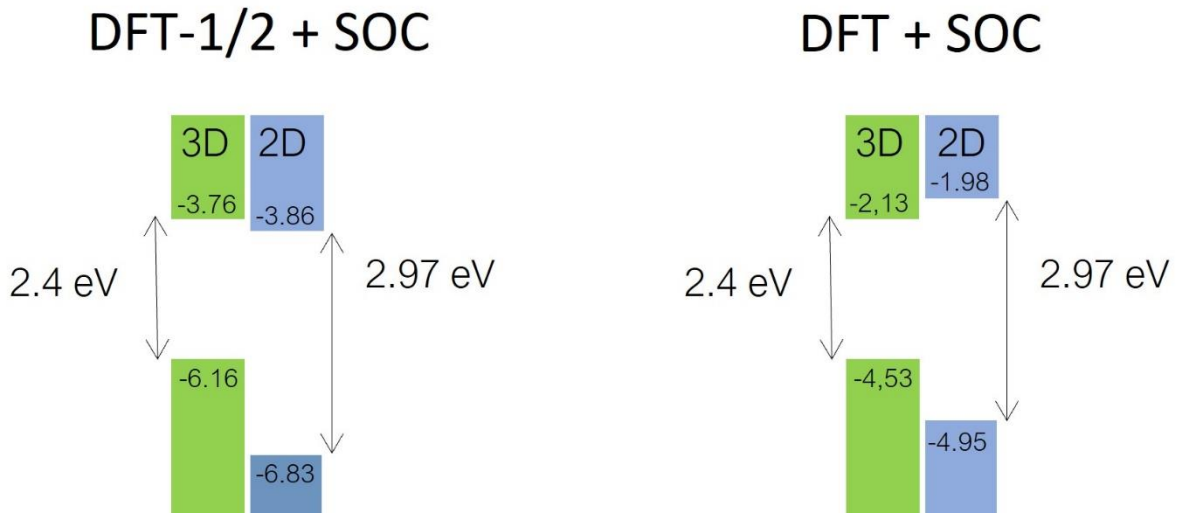

Figure S27 – Plot showing the predicted values of band energy levels of 3D CsPbBr3 (green) and 2D $BA_2CsPb_2Br_7$ (blue) calculated using single-point calculations with DFT-1/2 (left) and GGA-PBE (right), including spin-orbit coupling, and using experimental optical band gaps.

	a (Å)	b (Å)	c (Å)	α (°)	β (°)	γ (°)
orth-$CsPbBr_3$	8.44	11.61	7.88	90.0000	90.0000	90.0000
$BA_2CsPb_2Br_7$	39.32	8.08	8.22	90.0000	89.9976	89.9999

Table S5 – Structural parameters of the DFT optimized bulk structures of $CsPbBr_3$ and $BA_2CsPb_2Br_7$.

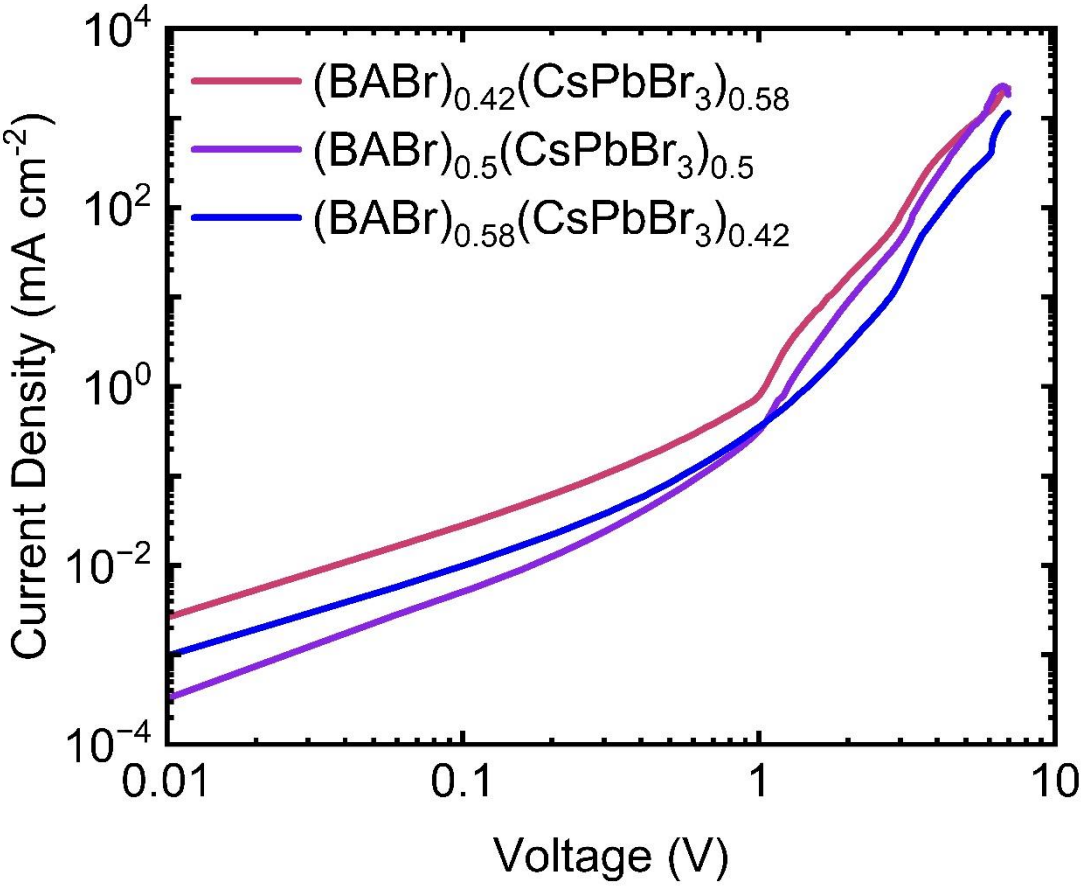

Figure S28 – Hole only unipolar current injection measurements of $BABr_x(CsPbBr_3)_{1-x}$ compositions. We were unable to fabricate working devices for other compositions and electron only devices outside of that shown in the main text.

References

(1) de Mello, J. C.; Wittmann, H. F.; Friend, R. H. An Improved Experimental Determination of External Photoluminescence Quantum Efficiency. *Advanced Materials* **1997**, *9* (3), 230–232. https://doi.org/10.1002/adma.19970090308.

(2) Ashiotis, G.; Deschildre, A.; Nawaz, Z.; Wright, J. P.; Karkoulis, D.; Picca, F. E.; Kieffer, J. The Fast Azimuthal Integration Python Library: PyFAI. *J Appl Cryst* **2015**, *48* (2), 510–519. https://doi.org/10.1107/S1600576715004306.

(3) Kohn, W.; Sham, L. J. Self-Consistent Equations Including Exchange and Correlation Effects. *Phys. Rev.* **1965**, *140* (4A), A1133–A1138. https://doi.org/10.1103/PhysRev.140.A1133.

(4) Soler, J. M.; Artacho, E.; Gale, J. D.; García, A.; Junquera, J.; Ordejón, P.; Sánchez-Portal, D. The SIESTA Method for Ab Initio Order-N Materials Simulation. *J. Phys.: Condens. Matter* **2002**, *14* (11), 2745. https://doi.org/10.1088/0953-8984/14/11/302.

(5) Cooper, V. R. Van Der Waals Density Functional: An Appropriate Exchange Functional. *Phys. Rev. B* **2010**, *81* (16), 161104. https://doi.org/10.1103/PhysRevB.81.161104.

(6) Hamada, I.; Otani, M. Comparative van Der Waals Density-Functional Study of Graphene on Metal Surfaces. *Phys. Rev. B* **2010**, *82* (15), 153412. https://doi.org/10.1103/PhysRevB.82.153412.

(7) Bitzek, E.; Koskinen, P.; Gähler, F.; Moseler, M.; Gumbsch, P. Structural Relaxation Made Simple. *Phys. Rev. Lett.* **2006**, *97* (17), 170201. https://doi.org/10.1103/PhysRevLett.97.170201.

(8) Troullier, N.; Martins, J. L. Efficient Pseudopotentials for Plane-Wave Calculations. *Phys. Rev. B* **1991**, *43* (3), 1993–2006. https://doi.org/10.1103/PhysRevB.43.1993.

(9) Basera, P.; Traoré, B.; Even, J.; Katan, C. Interfacial Engineering to Modulate Surface Dipoles, Work Functions and Dielectric Confinement of Halide Perovskites. *Nanoscale* **2023**, *15* (28), 11884–11897. https://doi.org/10.1039/D3NR01126G.

(10) Ferreira, L. G.; Marques, M.; Teles, L. K. Approximation to Density Functional Theory for the Calculation of Band Gaps of Semiconductors. *Phys. Rev. B* **2008**, *78* (12), 125116. https://doi.org/10.1103/PhysRevB.78.125116.

(11) Traoré, B.; Basera, P.; Ramadan, A. J.; Snaith, H. J.; Katan, C.; Even, J. A Theoretical Framework for Microscopic Surface and Interface Dipoles, Work Functions, and Valence Band Alignments in 2D and 3D Halide Perovskite Heterostructures. *ACS Energy Lett.* **2022**, *7* (1), 349–357. https://doi.org/10.1021/acsenergylett.1c02459.

(12) Fernández-Seivane, F.; Oliveira, M. A.; Sanvito, S.; Ferrer, J. On-Site Approximation for Spin–Orbit Coupling in Linear Combination of Atomic Orbitals Density Functional Methods. *J. Phys.: Condens. Matter* **2007**, *19* (48), 489001. https://doi.org/10.1088/0953-8984/19/48/489001.

(13) Stoumpos, C. C.; Malliakas, C. D.; Peters, J. A.; Liu, Z.; Sebastian, M.; Im, J.; Chasapis, T. C.; Wibowo, A. C.; Chung, D. Y.; Freeman, A. J.; Wessels, B. W.; Kanatzidis, M. G. Crystal Growth of the Perovskite Semiconductor CsPbBr 3 : A New Material for High-Energy Radiation Detection. *Crystal Growth & Design* **2013**, *13* (7), 2722–2727. https://doi.org/10.1021/cg400645t.

(14) Gong, X.; Voznyy, O.; Jain, A.; Liu, W.; Sabatini, R.; Piontkowski, Z.; Walters, G.; Bappi, G.; Nokhrin, S.; Bushuyev, O.; Yuan, M.; Comin, R.; McCamant, D.; Kelley, S. O.; Sargent, E. H. Electron–Phonon Interaction in Efficient Perovskite Blue Emitters. *Nature Mater* **2018**, *17* (6), 550–556. https://doi.org/10.1038/s41563-018-0081-x.
(15) Chen, H.; Lin, J.; Kang, J.; Kong, Q.; Lu, D.; Kang, J.; Lai, M.; Quan, L. N.; Lin, Z.; Jin, J.; Wang, L.; Toney, M. F.; Yang, P. Structural and Spectral Dynamics of Single-Crystalline Ruddlesden-Popper Phase Halide Perovskite Blue Light-Emitting Diodes. *Science Advances* **2020**, *6* (4), eaay4045. https://doi.org/10.1126/sciadv.aay4045.
(16) Even, J.; Pedesseau, L.; Katan, C. Understanding Quantum Confinement of Charge Carriers in Layered 2D Hybrid Perovskites. *ChemPhysChem* **2014**, *15* (17), 3733–3741. https://doi.org/10.1002/cphc.201402428.
(17) Traore, B.; Pedesseau, L.; Assam, L.; Che, X.; Blancon, J.-C.; Tsai, H.; Nie, W.; Stoumpos, C. C.; Kanatzidis, M. G.; Tretiak, S.; Mohite, A. D.; Even, J.; Kepenekian, M.; Katan, C. Composite Nature of Layered Hybrid Perovskites: Assessment on Quantum and Dielectric Confinements and Band Alignment. *ACS Nano* **2018**, *12* (4), 3321–3332. https://doi.org/10.1021/acsnano.7b08202.